Cell

Article

Condensate interfacial forces reposition DNA loci and probe chromatin viscoelasticity

Graphical abstract

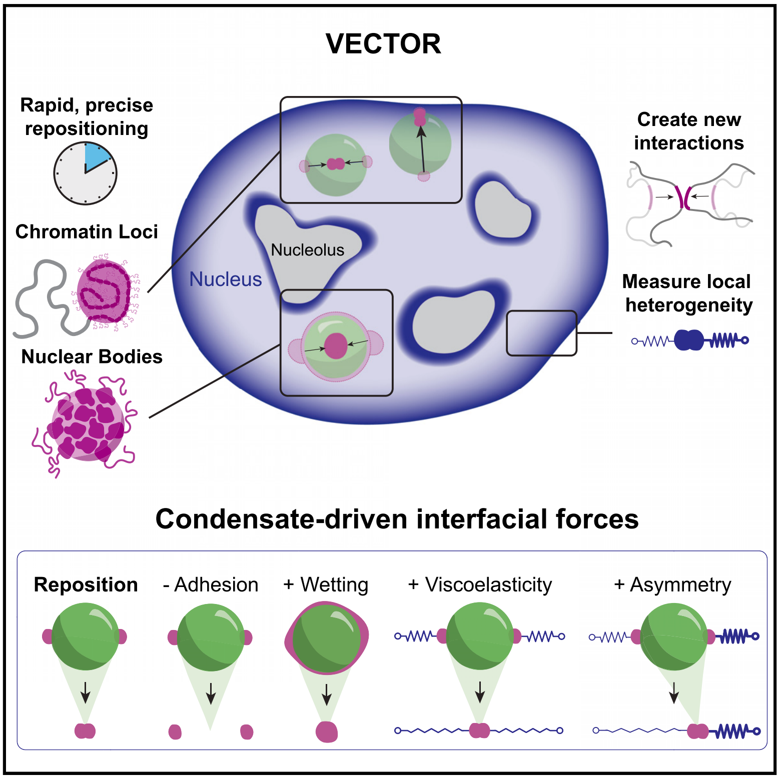

Authors

Amy R. Strom, Yoonji Kim,
Hongbo Zhao, ..., Andrej Košmrlj,
Cornelis Storm, Clifford P. Brangwynne

Correspondence

cbrangwy@princeton.edu

In brief

Measuring condensate formation and dissolution in cells reveals that the processes can generate as much force as a molecular motor and provides insight into the material properties of the nucleoplasm.

Highlights

- VECTOR enables rapid, precise genome reorganization through condensate capillarity
- Engineered condensate interfaces exert force on programmable target loci
- DNA loci exhibit significant viscoelastic heterogeneity across nuclear positions
- Native condensates are likely sites of force generation without ATP-driven motors

Strom et al., 2024, Cell *187*, 5282–5297
September 19, 2024 © 2024 The Authors. Published by Elsevier Inc.
https://doi.org/10.1016/j.cell.2024.07.034

CellPress

CellPress
OPEN ACCESS

Cell

Article

Condensate interfacial forces reposition DNA loci and probe chromatin viscoelasticity

Amy R. Strom,[1,9] Yoonji Kim,[2,9] Hongbo Zhao,[1,3,4] Yi-Che Chang,[5] Natalia D. Orlovsky,[2] Andrej Košmrlj,[3,4,6] Cornelis Storm,[7] and Clifford P. Brangwynne[1,4,6,8,10,*]
[1]Department of Chemical and Biological Engineering, Princeton University, Princeton, NJ 08544, USA
[2]Department of Molecular Biology, Princeton University, Princeton, NJ 08544, USA
[3]Department of Mechanical and Aerospace Engineering, Princeton University, Princeton, NJ 08544, USA
[4]Omenn-Darling Bioengineering Institute, Princeton University, Princeton, NJ 08544, USA
[5]Department of Chemistry, Princeton University, Princeton, NJ 08544, USA
[6]Princeton Materials Institute, Princeton University, Princeton, NJ 08544, USA
[7]Eindhoven University of Technology, Department of Applied Physics and Science Education, Eindhoven, the Netherlands
[8]Howard Hughes Medical Institute, Chevy Chase, MD 21044, USA
[9]These authors contributed equally
[10]Lead contact
*Correspondence: cbrangwy@princeton.edu
https://doi.org/10.1016/j.cell.2024.07.034

SUMMARY

Biomolecular condensates assemble in living cells through phase separation and related phase transitions. An underappreciated feature of these dynamic molecular assemblies is that they form interfaces with other cellular structures, including membranes, cytoskeleton, DNA and RNA, and other membraneless compartments. These interfaces are expected to give rise to capillary forces, but there are few ways of quantifying and harnessing these forces in living cells. Here, we introduce viscoelastic chromatin tethering and organization (VECTOR), which uses light-inducible biomolecular condensates to generate capillary forces at targeted DNA loci. VECTOR can be utilized to programmably reposition genomic loci on a timescale of seconds to minutes, quantitatively revealing local heterogeneity in the viscoelastic material properties of chromatin. These synthetic condensates are built from components that naturally form liquid-like structures in living cells, highlighting the potential role for native condensates to generate forces and do work to reorganize the genome and impact chromatin architecture.

INTRODUCTION

Biomolecular condensates are membraneless assemblies that form within living cells through liquid-liquid phase separation and related phase transitions.[1,2] These include P granules,[3] T cell receptor clusters,[4] stress granules,[5] the pyrenoid,[6] and nucleoli,[7] many of which physically interact with other cellular structures. Within the nucleus, chromatin-associated condensates are involved in nuclear functions, including chromatin remodeling,[8] transcriptional activation,[9,10] or repression[11] of specific euchromatic sequences, and formation and silencing of heterochromatin domains.[12–14] Aberrant spatiotemporal regulation of chromatin-interacting condensates is associated with diseased states.[8,15,16]

Decades of work in soft (non-living) matter show how the processes of nucleation, growth, and coarsening can be impacted by structured environments.[17,18] Studies suggest a role for related effects in living cells, including the interactions between condensates and viscoelastic environments including the cytoskeleton,[19,20] chromatin,[21] and the nuclear F-actin network of *Xenopus laevis* oocytes.[22] In the nucleus, condensates form in mechanically softer regions,[23] and chromatin organization impacts condensate coarsening dynamics.[24,25] Thus, the material state of the cell, particularly the nuclear interior, impacts the formation, positioning, and organization of condensates.

While the material state of chromatin influences functions including replication, transcription, and protection from DNA damage,[26] there is no consensus model describing this material state. Several studies suggest that chromatin behaves as a solid on the mesoscale,[27,28] while others have suggested a liquid-like state.[29,30] Existing intranuclear reorganization techniques have informed functional outcomes of nuclear (re)positioning and alteration of pairwise genomic contacts,[31–36] but there are extremely few techniques for direct force-response measurements utilizing local force application on singular chromatin loci.[30]

In considering possible methods of generating and harnessing forces within living cells, it is noteworthy that interfacial (surface) tension between immiscible phases can give rise to capillary forces.[7,23,37–39] These mechanical forces arise from energetically unfavorable non-spherical condensates, which can decrease free energy by rounding up into a sphere to minimize interfacial area. Recent studies have shown that model condensate systems exhibit interfacial forces that drive intracellular restructuring.[19,20,40,41] Therefore, condensates could function in a manner analogous to molecular motors,[37] applying picoNewton (pN)-level forces to intracellular objects; instead of utilizing ATP hydrolysis, forces would result from free energy stored in interfaces. By exploiting such condensate-driven interfacial interactions in the nucleus, it could be possible to probe local chromatin material properties and uncover principles of genome organization and function. However, there are currently no techniques for measuring and controlling interfacial forces in living cells.

Here, we introduce ViscoElastic Chromatin Tethering and ORganization (VECTOR), a system that creates interfacial interactions between an inducible synthetic condensate and target chromatin loci to apply a pulling force on the attached loci during condensate dissolution, resulting in their repositioning. Locus repositioning is rapid (~2 min), specific, and precise over micron distances. We combine analytical simulations to understand the work done through interfacial interactions and quantitatively estimate differential viscoelasticity across chromatin regions. Additionally, we demonstrate the versatility of the VECTOR platform through automation for high-throughput locus repositioning, force generation through a variety of synthetic condensate identities, dCas9-based programmable repositioning of both telomeric and non-telomeric sequences, as well as strategies for condensate-interface mediated repositioning of nuclear bodies. Together, these studies build a more complete understanding of internal mechanical properties and processes in the nucleus and provide a powerful toolkit for the study of cellular organization and function.

RESULTS

VECTOR: A rapid and precise system for chromatin locus repositioning in living nuclei

To engineer condensate capillarity, we leveraged our earlier work demonstrating light-dependent condensate induction in the nucleus.[23,40,42] We induced condensates in cultured human osteosarcoma U2OS cells with the two-component Corelet system,[42] composed of an iLID-GFP-Ferritin 24-mer "core" and an SspB-tagged phase separation-prone intrinsically disordered region (IDR). Upon 488 nm light exposure, improved light-induced dimer (iLID) and SspB interact, decorating each core with up to 24 sticky IDRs and triggering intracellular phase separation. By fusing the same IDR (e.g., FUS_N) to a tethering protein that binds a particular chromatin locus, in this case, the TRF1 protein that binds to repetitive telomeric TTAGGG sequences,[43] we promoted interactions between the "condensate module" (constructs that create the condensate) and the "adhesion module" (constructs that create interaction between the condensate and chromatin locus) (Figures 1A and 1B).

By directing blue light to a small region within the nucleus (1.2 μm diameter circle), we can readily nucleate condensates at tagged loci. With sustained light activation, condensates tethered to two nearby chromatin loci grow and coalesce into one, remaining associated with the target loci. Upon deactivation, the condensate shrinks, leading to a pulling force that repositions the loci (Figure 1A). In this example cell, we performed two simultaneous repositionings (Figures 1B and S1A; Video S1). With this localized light activation protocol, we achieved loci-spanning condensates with diameters up to 3 μm, enabling successful repositioning of telomeres across multiple microns of nuclear space. However, the probability of condensate merging reduces significantly if loci are separated by more than 2 μm (Figure 1C), a limitation set by achievable size of the loci-spanning condensate, which could be tuned through construct expression levels.

Tracking telomere position during the light activation/deactivation sequence reveals their capillary-force-dependent movement. We observe a jump together when the two loci-associated condensates merge (0.72 μm/min), then the loci follow the receding condensate surface as it shrinks (1.18 μm/min). Directed locus repositioning occurs over 1–2 min as the synthetic condensate dissolves, and the loci maintain their new positions for minutes after the condensate is dissipated, indicating successful long-term repositioning (Figure 1D). Notably, these micron-scale, rapid, and directed movements are achieved without use of ATP-driven motors—the most commonly described source of intracellular force generation. Instead, the forces underlying movement of these genomic loci are generated through capillary forces[37] at the interface between the condensate and chromatin locus. The scale of the capillary force is set by the relevant interfacial tension(s), which represents an energetic cost per unit area, with forces generated from surface area minimization.[37] Measurements to date on simplified *in vitro* systems,[7,44,45] and in some cellular contexts,[7,25] suggest condensate interfacial tensions in the range of 10^{-7}–10^{-3} N/m.[44]

The data shown above rely on cell-specific, user-defined regions of light activation/deactivation, an approach limited in throughput capacity. To increase throughput while maintaining specificity and precision, we tested a series of automated protocols that incorporate real-time feedback into regions of interest (ROI) generation for light patterning (see STAR Methods; Figures S1B–S1E). Global activation creates temporally controllable but small condensates that fail to merge (Figure S1B, "global" map of possible outcomes shown in Figure S1F). A thinner activation region induces larger condensates, and sliding this activation box promotes condensate fusion, but this approach is slow ($t > 60$ min per frame) due to the numerous sequential activation/deactivation cycles required (Figure S1B, "sliding box"). A square lattice pattern of punctate activation regions creates condensates that occasionally merge but are not all associated with target loci (Figure S1B "array").

Considering these limitations, we designed an approach that uses real-time image analysis feedback to identify nearby telomere pairs, then creates activation regions connecting them (Figure S1C). Bright spot detection followed by activation between nearby pairs is consistent and efficient, resulting in at least one pair of loci associated with the same condensate in 46% of cells (81 out of 176 nuclei attempted) and leading to scalability and successful repositioning in 64% of those nuclei (52 out of 81 potential locus pairs) in less than 5 min per field of view (Figure S1D; example kymographs in Figure S1E; map of potential

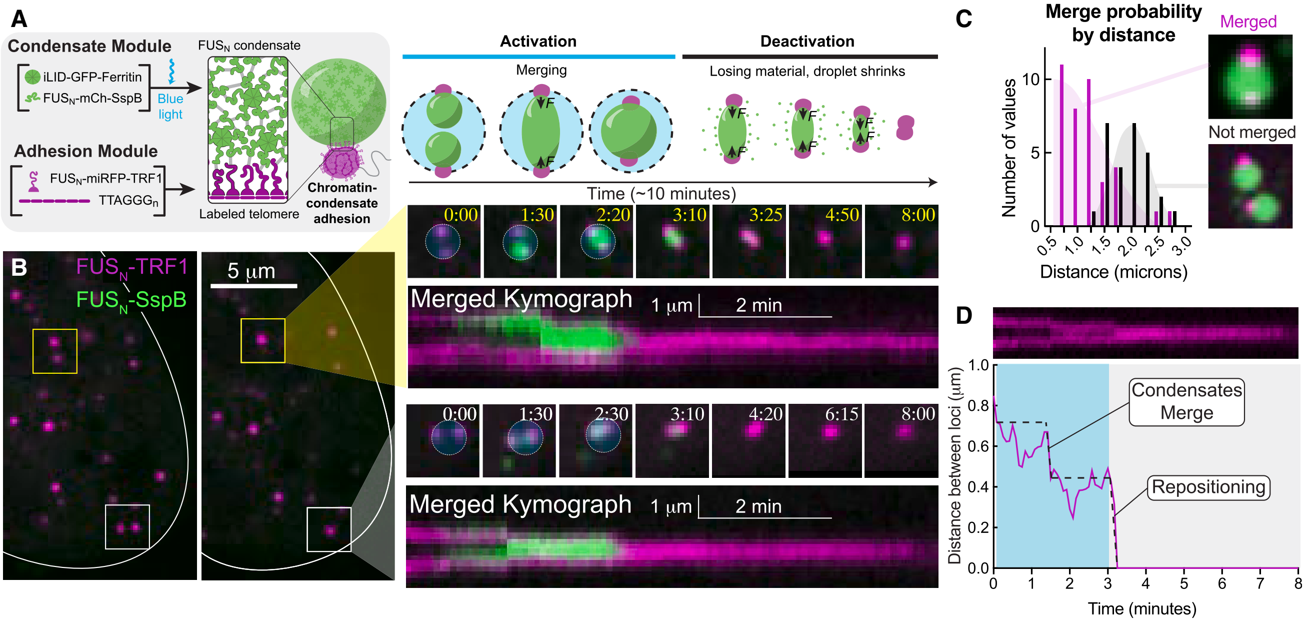

Figure 1. A light-inducible system for rapid, precise repositioning of chromatin loci

(A) Schematic of VECTOR constructs that create a light-inducible condensate (condensate module, green) and adhesion between the condensate and chromatin locus (adhesion module, magenta). By applying a localized light activation-deactivation pattern (blue circular ROI), locus-attached condensates grow, merge, and shrink, pulling loci together. Force is applied (*F*, black arrows) during merging and light deactivation.

(B) Two pairs of telomeres were targeted, boxed in white and yellow (see also Figure S1A). Light activation (blue circle) triggers FUS$_N$-SspB synthetic condensate formation at targeted loci. Stills from the boxed areas show condensates (FUS$_N$-SspB, green) growing at the locally activated loci (1:30), merging (2:20–2:30), repositioning the attached loci as the condensate shrinks (3:10–4:20), and the loci remain for the duration of the time series (8:00). Kymographs demonstrate this process over continuous time.

(C) A histogram of distances between loci pairs that fused (magenta) or not (black). n = 38 merged, 29 not merged locus pairs.

(D) Graph of the distance between target loci over time. Blue shading indicates light activation.

See also Figure S1 and Video S1.

outcomes in Figure S1F). These data exemplify how condensates can be harnessed to rearrange intracellular objects without the use of ATP-driven motors.

Adhesion between condensate and chromatin is essential for precise force application

We hypothesized that capillary forces are transmitted to the target chromatin locus by adhesion between the shrinking FUS$_N$ condensate and the FUS$_N$-coated telomere surface. We performed the same light activation/deactivation protocol in cells expressing a chromatin-bound fluorescent protein that has no interaction with the condensate (miRFP670-TRF1) (Figures 2A and 2B), and no sustained force was exerted on the loci, as expected (Figure 2C; Video S2).

The small expansion and contraction of the distance between chromatin loci (Figure 2C) may be due to the condensate itself displacing the chromatin network between the loci. Marking all DNA with a silicon rhodamine (SiR)-DNA dye shows that bulk chromatin is excluded from the condensate (Figure S2A), consistent with previous studies.[23,24] The distance between two nuclear locations (yellow arrows, Figure S2A) over time increases slightly during activation and recovers to the original distance during condensate dissolution (Figure S2B). These data suggest that the movement of chromatin loci not adhered to the condensate is due to bulk material displacement, and precise repositioning of loci depends on interfacial interaction with the condensate.

The amino acids that contribute to self-interaction underlying phase separation of FUS$_N$ have been extensively studied,[46,47] revealing that the 27 tyrosines of FUS$_N^{WT}$ act as "sticker residues" separated by "spacer residues" (Figure 2D). To examine the role of tyrosines in facilitating chromatin-condensate adhesion, we created FUS$_N$-miRFP670-TRF1 constructs with 3, 5, 9, 15, or 27 tyrosine-to-serine mutations (Y-to-S, Figures 2D–2F) and asked whether these mutations altered adhesion to the wild-type (WT) condensate by measuring the detachment probability. Single locus-condensate interactions were determined to be adhered or detached based on whether the telomere and condensate maintained contact or not during condensate dissolution (Figure 2E).

Detachment of FUS$_N^{WT}$-tagged telomeres from FUS$_N^{WT}$ condensates is extremely rare, with 0 out of 33 loci detached (0% detachment rate, Figure 2F). Detachment becomes more likely with increasing number of Y-to-S mutations, resulting in 88% detachment rate for the FUS$_N^{27YS}$-miRFP670-TRF1 construct (Figure 2F), suggesting tyrosines mediate almost all of the FUS$_N^{WT}$ adhesion strength, which arises from an estimated several hundred IDR-IDR interactions (see STAR Methods). If

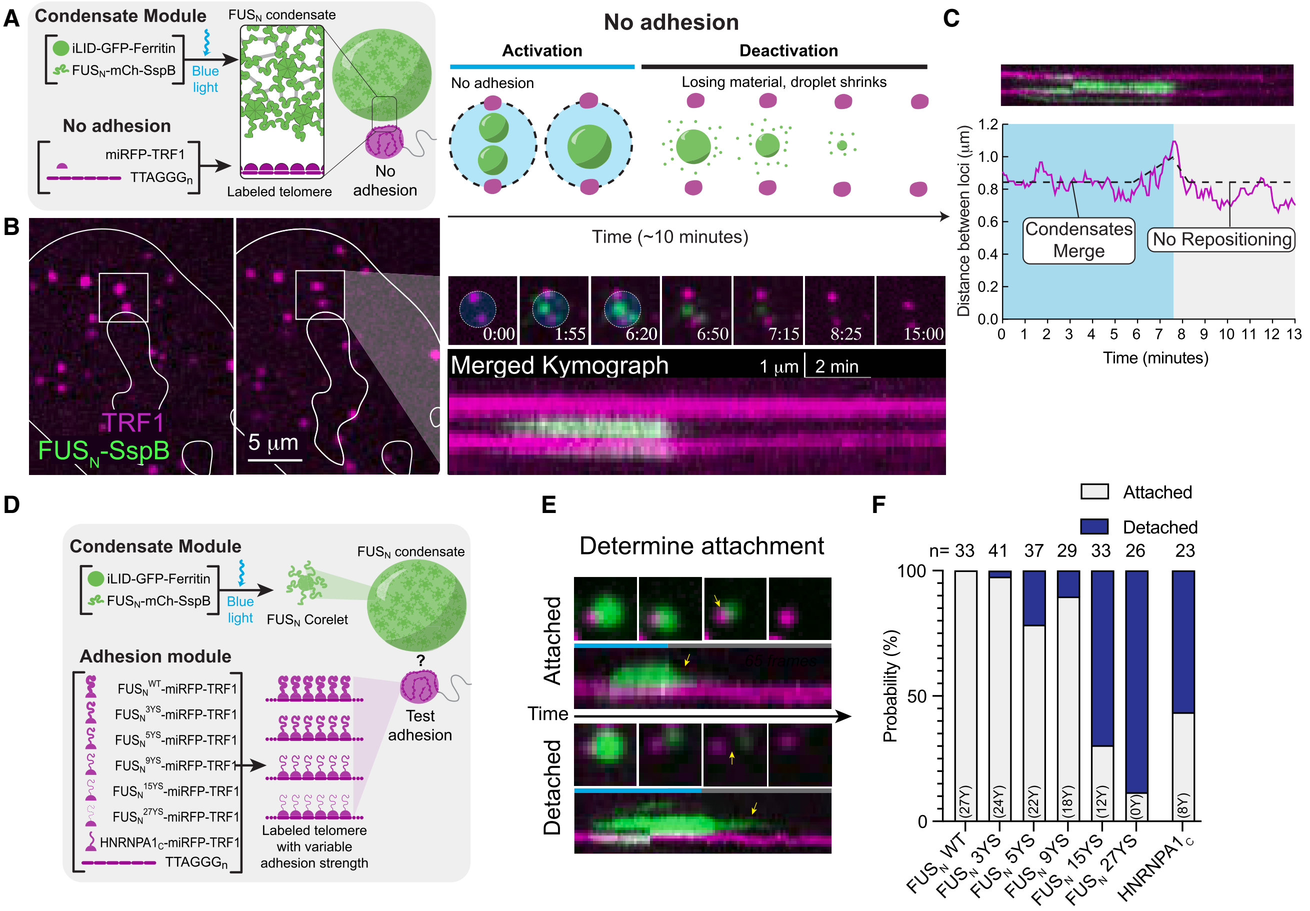

Figure 2. Chromatin-condensate adhesion is required for repositioning

(A) Schematic of constructs with no adhesion. TRF1 binds telomeric TTAGGG repeats but does not have any added IDR.

(B) Stills and kymograph of a no-adhesion example. Condensates grow (1:55) and fuse (6:20) but do not reposition the chromatin loci (6:50–15:00).

(C) Graph of the distance between two telomeres without condensate adhesion.

(D) Schematic of altered adhesion constructs of telomere-bound FUS_N IDR with tyrosine-to-serine (YS) mutations.

(E) Locus-attached condensates were de-activated and classified as staying adhered if they maintained contact with the locus (top) or as detached if they lost contact (bottom).

(F) Quantification of the number of adhered and detached chromatin-condensate pairs with increasing Y-to-S mutations. n indicated above each bar represents individual locus-condensate interactions. Trend is statistically significant by chi-squared test for trend, $p = 0.0001$.

See also Figure S2 and Videos S2 and S3.

the number of tyrosines is deterministic of the adhesion strength for a distinct pair of sequences, $HNRNPA1_C$, an orthogonal IDR that contains 8 tyrosines and has been reported to interact weakly with FUS_N,[43,48] should have a detachment rate of about 80%. However, we find only 13 out of 23 (56%) detach, suggesting that spacing of tyrosines, neighboring amino acid context, and other sequence features contribute to intermolecular interaction strength, consistent with previous reports.[49]

Until this point, we have utilized a specific IDR, FUS_N, to mediate interfacial force generation. Capillary forces are a general feature of condensates, so we next sought to create a condensate module with adaptable sequence identity. We replaced FUS_N in the condensate module (FUS_N^{IDR}-mCh-SspB) with phase-separation-prone IDRs from DDX4 or BRD4 [X^{IDR}]-mCh-SspB and replaced the chromatin-tethered FUS_N IDR in the adhesion module (FUS_N^{IDR}-miRFP670-TRF1) with iLID (*iLID*-miRFP670-TRF1),[40] which recruits [X^{IDR}]-mCh-SspB upon light activation (Figures S2C and S2D). Similar to the FUS_N system, during light activation, chromatin loci remain adhered to the [X^{IDR}] condensate surface, and upon light deactivation, loci are repositioned (Figure S2D), confirming that non-FUS_N condensates can also apply force to adhered loci.

In addition to chromatin loci, other structures, including nuclear bodies, should be amenable to repositioning with VECTOR. We attempted to reposition Cajal bodies, native nuclear condensates associated with various aspects of RNA metabolism, using Coilin to generate the adhesion module FUS_N-miRFP670-Coilin (Figures S2E–S2G). Interestingly, when a FUS_N condensate forms at a Cajal body, FUS_N-miRFP670-Coilin distributes to cover the entire surface of the FUS_N condensate (Figures S2F and S2G).

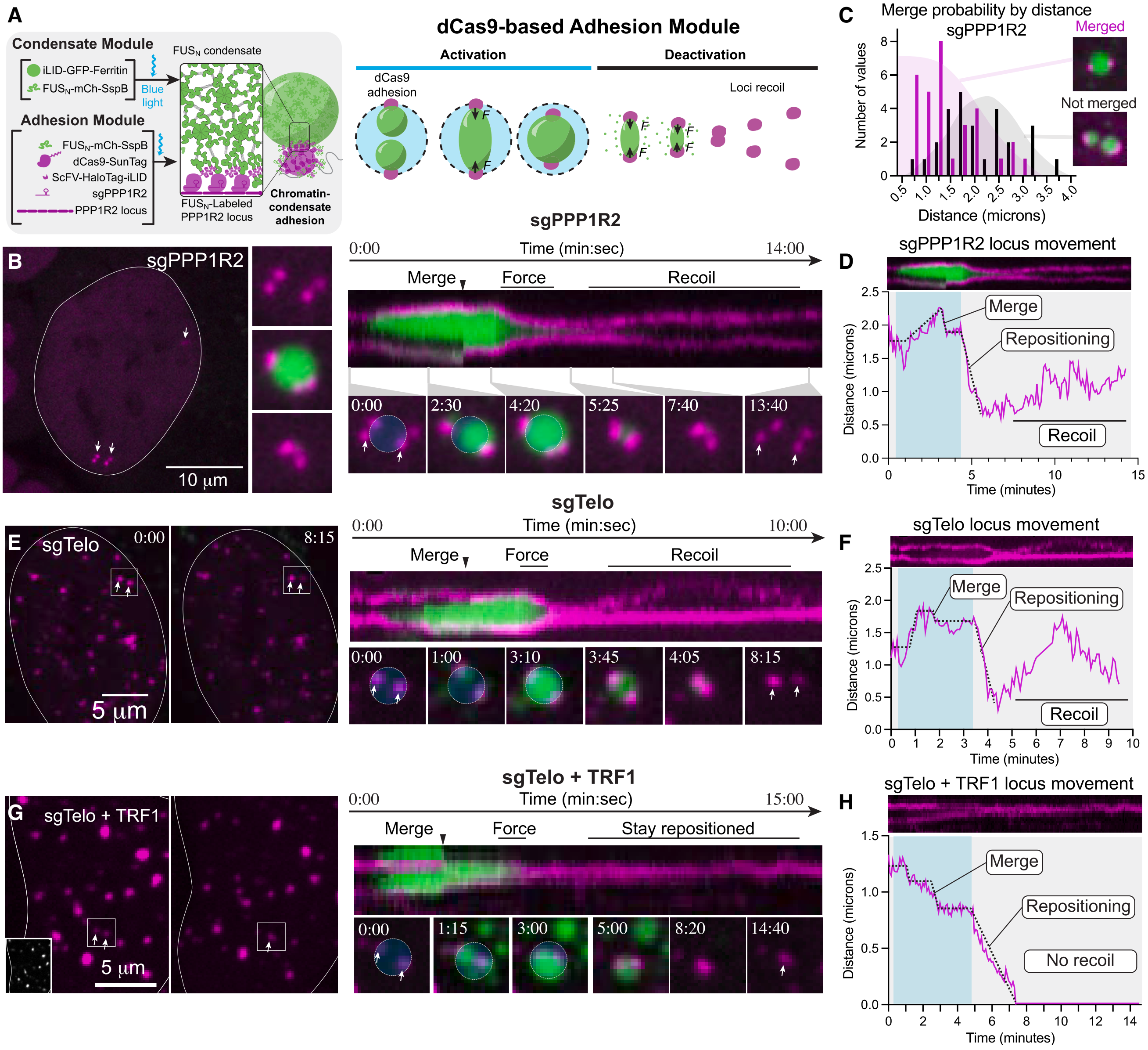

Figure 3. A dCas9-based adhesion module for repositioning non-telomeric loci

(A) Schematic of constructs used for dCas9-based VECTOR. Condensate module: as in Figure 1. Adhesion module: sgPPP1R2 single guide RNA targets dCas9-SunTag to repetitive PPP1R2 locus. scFv-HaloTag-iLID binds multivalent SunTag, and upon blue light FUS$_N$^{IDR}-mCh-SspB decorates iLID, creating adhesion between FUS$_N$-labeled PPP1R2 locus and FUS$_N$ condensate.

(B) Representative images and kymograph of PPP1R2 loci repositioned using dCas9-based adhesion module.

(C) A histogram of distances between pairs of PPP1R2 loci separated by whether the locus-attached condensates merge (magenta) or not (black). n = 31 merged, 27 not merged loci pairs.

(D–H) (D) Graph of the distance between two PPP1R2 loci over time; note recoil. Representative images, kymograph (E), and distance graph (F) of telomeric loci repositioned using dCas9-based adhesion module with sgTelo telomeric sequence targeting guide RNA. Note locus recoil. Representative images, kymograph (G), and distance graph (H) of telomeres repositioned using dCas9-based adhesion module with TRF1 overexpression.

See also Figure S3 and Video S4.

Nevertheless, from two original Cajal bodies, only one remains after deactivation, indicating successful repositioning (Figure S2F; Video S3). These data demonstrate that capillary forces are generated by IDR-IDR interactions and can reposition native nuclear condensates in addition to chromatin loci.

A dCas9-based approach to generate force on non-telomeric genomic elements

Next, we sought to extend our intranuclear force generation approach to non-telomeric chromosomal loci using a dCas9-based adhesion module (Figure 3A).[23] We targeted PPP1R2, a repetitive locus of ~500 copies on Chr3q29, which enables binding of many dCas9 molecules using a single guide RNA (sgRNA). In this dCas9-based system, the condensate module is the same light-inducible FUS_N Corelet as described above. The adhesion module is made of four components that target the repetitive locus: (1) a small guide RNA complementary to the target locus, and (2) dCas9 covalently linked to a SunTag, which has 24 copies of a binding site for viral protein ScFv. We covalently link (3) ScFv to HaloTag (for visualization) and iLID such that when blue light is activated, (4) FUS_N-mCh-SspB binds ScFv-HaloTag-iLID, creating a dCas9-targeted telomeric locus decorated with FUS_N. Precise stoichiometry between the four adhesion module components was essential for locus-specific labeling in this dCas9-based VECTOR implementation (see STAR Methods). sgRNA targeting of PPP1R2 results in three puncta in pseudotriploid U2OS cells during G1 (Figure 3B) and up to six puncta in G2 after DNA replication. As with telomeres, PPP1R2 loci within 2 μm of each other are most likely to achieve productive bivalent condensate attachment (Figure 3C), and condensate dissolution applies force to move PPP1R2 loci toward each other (Figure 3D). While the dCas9-based adhesion module is overall more detachment-prone than the FUS_N-TRF1-based adhesion module, the lower number of repeats bound by sgPPP1R2 (~500 copies per locus) only slightly increases the detachment probability compared with a dCas9 adhesion module that uses a telomeric $TTAGGG_n$-targeting sgRNA (sgTelo, >1,000 copies per locus). The sgTelo module exhibits 15/57 or 27% detachment, while the sgPPP1R2 module exhibits 24/75 or 32% detachment (Figures S3A–S3C), suggesting that 500 binding sites are sufficient for force generation at the PPP1R2 locus.

Interestingly, PPP1R2 loci repositioned using the dCas9 adhesion module recoil toward their original positions after condensate dissolution (Figures 3B and 3D; Video S4), unlike telomere loci repositioned using the TRF1 adhesion module (Figures 1, S2C, and S2D; Video S1). These disparate recoil behaviors may be due to (1) differences in the force application systems, (2) end vs. internal chromosomal location, or (3) other physical characteristics disparate between these loci. We measured recoil probability with the dCas9-based adhesion module targeting telomeres, expecting that if chromosomal positioning or other physical characteristics control recoil behavior, telomeres will remain in their repositioned locations, while if differences in the adhesion modules control recoil behavior, telomeres will recoil similar to the PPP1R2 loci.

Telomeres repositioned via the dCas9 adhesion module recoil after force application, similar to PPP1R2 loci (Figures 3E and 3F). We examined whether overexpression of TRF1 in combination with the dCas9 sgTelo adhesion module would prevent recoil (Figures 3G and 3H). Indeed, while PPP1R2 loci and telomeres repositioned with the dCas9 adhesion module recoil after force application in more than 90% of cases (16 out of 17 locus pairs recoil in sgPPP1R2; 17 out of 18 locus pairs recoil in sgTelo), sgTelo-labeled telomeres only recoil in 50% of cases when TRF1 was also overexpressed (8 out of 16 locus pairs recoil). This suggests that the apparent liquid-like coalescence of telomeres[40] is impacted by stoichiometry of shelterin complex components and is consistent with previous reports that non-stoichiometric expression of TRF1 can lead to aberrant telomere clustering and telomeric DNA fusions.[40,50,51]

Notably, during light activation, dCas9-labeled PPP1R2 loci extend to coat the surface of the condensate, while FUS_N-miRFP670-TRF1-labeled loci remain punctate (Figure S3D). This observation may reflect differences in the internal cohesion, mechanical properties, or condensate wetting behavior of these structures (see schematic Figure S3E). Overall, these findings suggest that chromatin-bound IDR-containing proteins mediate stable contacts between distal chromosomal loci, consistent with 3D genome mapping results implicating IDRs in long-range interactions.[52]

Chromatin is a viscoelastic liquid with mesoscale heterogeneity

The material state of the nuclear interior is technically difficult to probe, and previous measurement methods include confounding contributions from the nuclear lamina and envelope, as with micropipette manipulation of whole nuclei,[53] or atomic force microscopy (AFM) compression.[54] We sought to perform direct active rheological measurements from within the nucleus with VECTOR, then observe detachment rates and post-detachment locus recoil trajectories, which yield insight into relaxation behaviors of mechanically stressed chromatin (Figure 4A).

If chromatin behaves as a purely elastic material, we expect locus-condensate detachment most often when the locus is moved far from its initial position, when the strain is highest. We measured the probability of locus detachment as a function of strain, where d_0 is the initial distance between two loci, and d_d is the distance between loci under force, so dimensionless strain is defined by fractional deformation $(d_0 - d_d)/d_0$ but did not observe a strain-dependent trend (Figure S4A). This suggests that chromatin is not a purely elastic material but rather exhibits fluid-like dissipation. Materials with partially liquid-like behavior are characterized by stresses that depend not only on the magnitude of deformation but also on the rate of change of deformation (e.g., velocity or strain rate). With VECTOR, the moving locus follows the receding condensate surface during light deactivation; therefore, velocity is dependent on the rate of condensate diameter shrinking, which we observed to range between 0.1 and 1.2 μm/min. Chromatin loci attached to condensates with full adhesion strength (FUS_N^{WT}-miRFP670-TRF1) did not detach from the shrinking condensate at any tested velocity, while loci attached by the very-weak-adhesion construct FUS_N^{15YS}-miRFP670-TRF1 showed a higher probability of detachment at a broad range of tested velocities, though this did not trend with velocity (Figure S4B). Loci attached with the moderately mutated construct FUS_N^{5YS}-miRFP670-TRF1 exhibited a velocity-dependent detachment, with detachments more frequent at lower velocities (Figure S4B; < 0.5 μm/min, chi-squared test trend ****$p = 0.0004$), a behavior not expected for purely elastic materials. We note that interpretation of velocity dependence is confounded by the fact that the pulling velocity is coupled to the size-dependent condensate dissolution rate. Nonetheless, these data point to chromatin exhibiting significant liquid-like properties rather than being a purely elastic material.

We next built an analytical simulation to examine the expected relative influence of elastic- and liquid-like chromatin properties

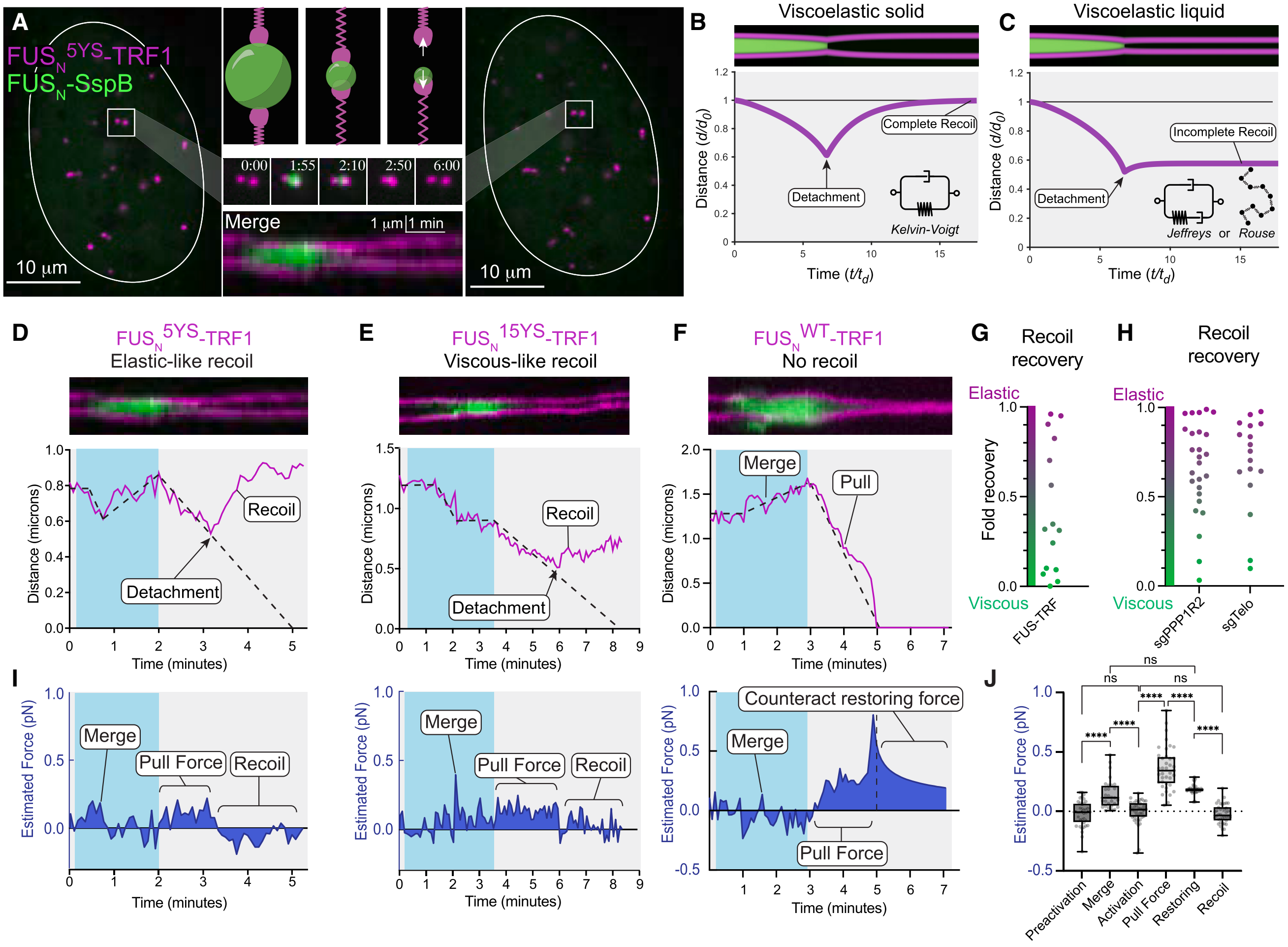

Figure 4. Simulations predict viscoelastic mechanical properties of chromatin repositioning

(A) VECTOR experiments using detachment-prone FUS$_N^{mut}$-miRFP670-TRF1 mutants result in detachment and recoil of the associated locus.

(B) Simulating locus detachment from a shrinking condensate and subsequent recoil with a viscoelastic solid (Kelvin-Voigt) model predicts that, during recoil, the chromatin loci always return to their original positions, as the energy of the elastic spring must be dissipated.

(C–E) (C) Simulating locus detachment and recoil in a viscoelastic liquid (Jeffreys or Rouse polymer) model predicts that the chromatin loci will not return all the way to their original positions, as some of the energy is dissipated through the viscous dashpot. Graphs of locus distance and estimated force over time from experiments in live cells show that some detachments result in elastic-like recoil (D), while others result in viscous-like recoil (E).

(F) Locus distance and estimated force over time in an example that does not detach.

(G and H) (G) Graph of locus' recovered distance normalized to their original position (fold recovery) for 15 loci pairs shows a wide spread of both viscous-like and elastic-like recoil behavior using both the TRF1 overexpression-based system and (H) dCas9-based system targeting telomeres (n = 26 loci pairs) or PPP1R2 (n = 17 loci pairs).

(I) Graphs of force experienced by loci, estimated with a calibrated Rouse polymer model (see STAR Methods), over experiment time for the elastic-like, viscous-like, and no recoil trajectories shown in (D)–(F).

(J) Average estimated force measurements for n = 25 loci pair trajectories during six experimental time windows. Error bars show standard deviation. $^{****}p \leq 0.0001$ by one-way ANOVA.

See also Figure S4 and Video S5.

on locus recoil behaviors. The simulation mimics dissolution-dependent repositioning by light-inducible condensates (green) wetting a second phase (magenta, representing the chromatin locus) (Figure 4B). The condensate forms upon light-induced association of the core and IDR, with the free energy of mixing defined by the Flory-Huggins theory.[55] As we observed experimentally, these simulations show that both condensate coalescence and dissolution lead to the associated loci moving toward each other (Figure S4C), with adhesion required for repositioning (Figure S4D). Additional characterization and parameters of these simulations are described in the method details (Figures S4E–S4M; Video S5).

The addition of linear viscoelasticity to this simulation imparts resistance to locus movement (Figures 4B and 4C). Starting with a system of two loci attached to a single condensate, we simulated the chromatin locus movement during the force of repositioning and considered the chromatin material to be either (1) a viscoelastic solid following the Kelvin-Voigt model, which anchors the locus at its original position by a spring and dashpot in parallel (Figure 4B, graph inset), or (2) a viscoelastic liquid following the Jeffreys model,[56] which adds a dashpot in series with the spring (Figure 4C, left graph inset), or the Rouse polymer model, based on polymer relaxation-controlled viscoelasticity[57–60] (Figure 4C, right graph inset and S4K–S4M). While these are not the only possible models of viscoelastic solids and liquids, we chose them as our initial models because they are the simplest and most well-known models that make qualitatively different predictions.

In the viscoelastic solid Kelvin-Voigt model, the single spring spanning the unit dictates that the loci will always return to their original positions (Figure 4B). By contrast, in the viscoelastic liquid Jeffreys or Rouse polymer models, a detached locus would not necessarily return all the way back to its original position (Figure 4C), since some of the energy is dissipated by viscous relaxation. This relaxation is governed by the dashpot in the Jeffreys model, where a short spring relaxation time compared with repositioning time implies less recoil, while within the molecular picture of the Rouse polymer model, it is governed by polymer relaxation timescales. We observed locus detachments with the $\text{FUS}_\text{N}^\text{5YS}$- and $\text{FUS}_\text{N}^\text{15YS}$-miRFP670-TRF1 weak-adhesion mutants (Figure 4A) and tracked post-detachment recoil behaviors. Interestingly, we observed both elastic-like recoil, with detached loci returning entirely to their original positions (Figure 4D), as well as viscous-like recoil, with detached loci returning only partially to their original positions (Figure 4E). Over 15 detachment and recoil events using the $\text{FUS}_\text{N}^\text{15YS}$-miRFP670-TRF1 mutant, we observed a wide spread of recoil recovery, with some loci presenting viscous-like recoveries (green, Figure 4G, bottom) and others presenting elastic-like recoveries (magenta, Figure 4G, top). Utilizing the dCas9-based adhesion module, we also observe a spread of recovery behaviors of PPP1R2 and telomeres (Figure 4H), consistent with the recoil dynamics reflecting intrinsic chromatin viscoelasticity.

We sought to estimate the magnitude of forces generated with VECTOR, building from a framework recently deployed to analyze intracellular force generation by magnetic tweezers.[30] In particular, we estimated forces during the light activation/deactivation sequence by calibrating a Rouse polymer model using telomere mean squared displacement (MSD) data, then calculating the fluctuating forces required to move loci on observed trajectories.[30] Here, the Rouse polymer model is used to represent force being applied at a point source along the chromatin polymer, which allows the system to be calibrated by passive microrheological approaches (see STAR Methods). This force estimation approach yields results on the order of ~0.36 pN during condensate dissolution (Figures 4D–4F, bottom), which is comparable to individual molecular motor forces (e.g., kinesin).[61] Note that force estimation is calculated based on the relative distance between two loci, with positive force indicating loci moving toward each other and negative force moving them apart. The force hovers around zero before condensate growth and during late activation when the condensate is not changing size (−0.02, −0.01 pN, respectively, Figure 4I "preactivation," "activation"), then spikes during condensate coalescence (0.15 pN, Figure 4I "merge") and exhibits sustained force during locus repositioning due to condensate dissolution (0.36 pN, Figure 4I "pull force," see STAR Methods). In examples where loci recoil after collision, the force drops to near-zero after detachment (−0.02 pN, Figure 4I "recoil"), while in examples where loci remain attached (Figure 4H), forces slowly decrease through viscous dissipation; this sets the scale of the minimum sustained adhesion required between chromatin-bound IDRs to counteract the restoring force of the viscoelastic medium (0.18 pN, Figure 4I "restoring").

Taken together, our data are most consistent with a viscoelastic liquid model of chromatin material state at the mesoscale that arises from Rouse polymer-like movement of the chromatin. However, the broad spread of recoil behaviors indicates significant heterogeneity in the viscoelastic response of the chromatin network.

Proximity to nuclear or nucleolar periphery influences chromatin viscoelasticity

We next sought to examine the origins of heterogeneity in chromatin viscoelasticity that may arise from differential organization states of heterochromatic and euchromatic regions of the nucleus. Tracking diffusion of telomere loci in U2OS cells every 3 s for 30 min and plotting their pairwise MSD trajectories reveals that telomeres exhibit sub-diffusive motion with an average exponent of $\alpha \approx 0.46$ (Figure S5A). This is close to a Rouse polymer model prediction of exponent $\alpha = 0.5$ and consistent with previous studies.[24,40,62] The nuclear periphery of most human cell types is enriched in heterochromatin,[63] the epigenetically methylated, densely compacted, and transcriptionally silenced regions of chromatin.[63] Since heterochromatin is more densely compacted and thus presumably stiffer than nuclear interior-localized euchromatin, we plotted these pairwise MSDs binned into two categories by their nuclear location (Figure S5A); pairs where both loci were located within 0.55 μm of the nuclear periphery were considered peripheral (blue), or pairs where both loci were located greater than 0.55 μm from any periphery were considered internal (mauve). Peripheral pairs exhibit slightly lower diffusion coefficient than internal pairs (peripheral $D = 0.001168\ \mu\text{m}^2/\text{s}^\alpha$, internal $D = 0.001316\ \mu\text{m}^2/\text{s}^\alpha$), consistent with previous reports[64] indicating higher viscoelastic resistance near the nuclear periphery, potentially due to heterochromatic state (Figure S5B).

Given these indications of heterochromatin-associated mechanical heterogeneity, we reasoned that we may be able to use VECTOR to quantify chromatin's mechanical heterogeneity across mesoscale (1–2 μm) nuclear regions. To examine this, we use simulations to predict the movement of chromatin loci across either mechanically homogeneous or heterogeneous systems (Figure 5A). We define a dimensionless parameter, ρ, which represents the mechanical resistance of the spring-and-dashpot viscoelastic system, with ρ_1 and ρ_2 indicating resistance of the two respective loci attached to a singular condensate. In the homogeneous case $\rho_2/\rho_1 = 1$, the viscoelastic parameters between the two loci are equal, which result in symmetric locus movement, each traversing 50% of the distance between them. By contrast, when the movement of loci is simulated in an heterogeneous system with unequal resistance ($\rho_2/\rho_1 = 5$), we

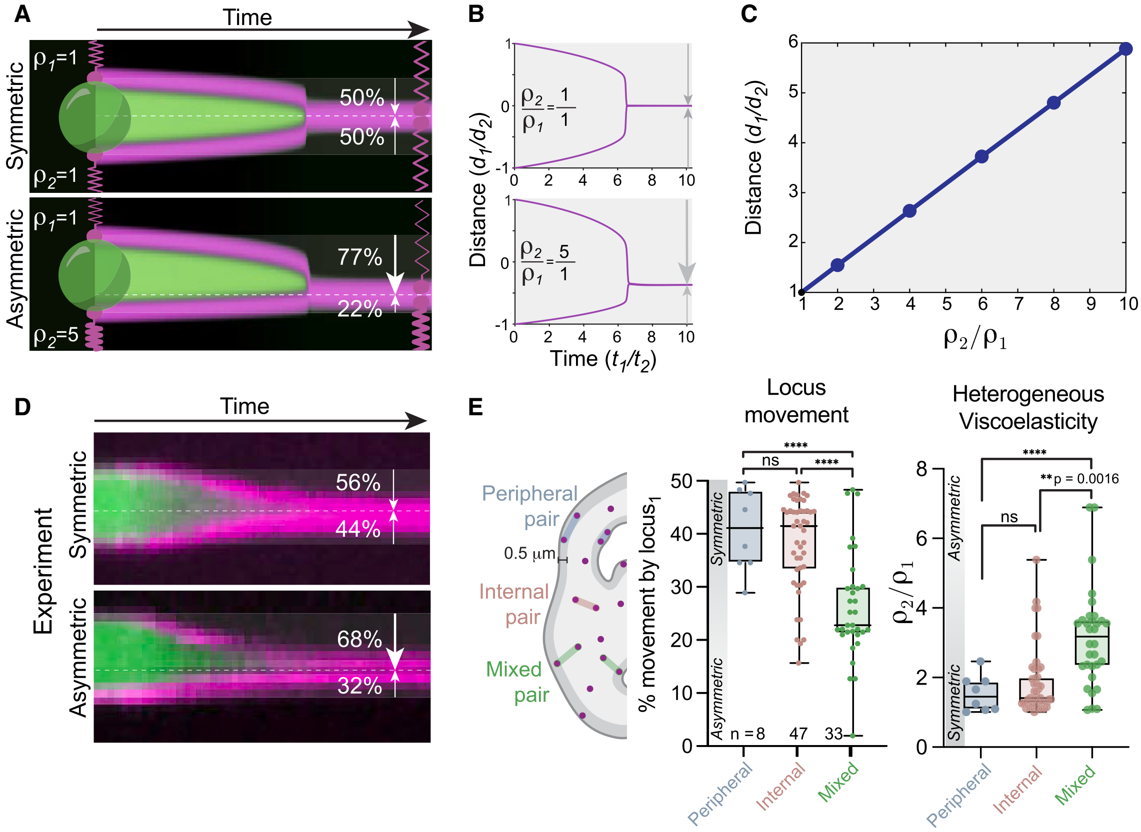

Figure 5. Proximity to nuclear or nucleolar periphery dictates local heterogeneity in chromatin viscoelasticity

(A) Simulations of shrinking condensates with equivalent viscoelastic resistance of the two attached loci ($\rho_2/\rho_1 = 1$) result in equal distance traveled by each locus (top; 50%, 50%), while simulations with unequal viscoelastic resistance ($\rho_2/\rho_1 = 5$) show unequal distance traveled by each locus (bottom; 77%, 22%).

(B) Plots of the loci positions over time in simulations of a symmetric (top) or asymmetric system (bottom).

(C) Graph describing the relationship between the ratio of viscoelasticity of two loci (ρ_2/ρ_1) and the ratio of the distance traveled by each locus (d_1/d_2).

(D) Experiment-derived kymographs of a symmetric VECTOR system (top) and an asymmetric VECTOR system (bottom).

(E) Quantification of asymmetric locus movement and resulting heterogeneous viscoelasticity in pairs of telomeres both < 0.5 µm from the periphery of nucleus or nucleolus (peripheral, blue, $n = 8$), both internal (mauve, $n = 47$), or one peripheral and one internal (mixed, green, $n = 33$). Box and whisker plot; box shows 25th, median, and 75th percentile; whiskers span minimum to maximum. Statistical significance was calculated using one-way ANOVA with multiple comparisons, ns, not significant. ****$p < 0.0001$.

See also Figure S5 and Video S6.

find asymmetric movement (77%, 22%; Figures 5A, bottom, and 5B). Simulations where $\rho_2/\rho_1 = 2, 4, 6, 8, 10$ reveal the linear relationship between differential viscoelastic properties and the ratio of distance traveled by each locus (d_2/d_1) (Figures 5C and S5C–S5K).

Consistent with local heterogeneity in mechanical response manifesting in unequal loci displacement, in experiments we frequently observe both symmetric (Figure 5D, top) and asymmetric (Figure 5D, bottom) movement of loci pairs using the FUS$_N$-TRF1 adhesion module (Video S6). Moreover, we find that when both loci are nuclear "internal" (> 0.5 µm from a nuclear or nucleolar periphery) or "peripheral" (< 0.5 µm from a nuclear or nuclear periphery), movement is relatively symmetric, while "mixed" pairs (one peripheral locus and one internal locus) are asymmetric (Figure 5E). Given the linear relationship between differential viscoelastic properties and the ratio of distance traveled by each locus established in simulations (Figure 5C), these data imply that mixed pairs connect loci from environments with greater heterogeneity ($\rho_2/\rho_1 \neq 1$; Figure 5E). Together, these results support a model of a viscoelastic liquid nuclear interior with an average of 3.1-fold increased resistance within 0.5 µm of nuclear and nucleolar peripheries.

Chromatin density and epigenetic state influence local chromatin viscoelasticity

Both DNA density and epigenetic state are thought to contribute to total nuclear mechanics[53,65] and could determine local mechanical heterogeneity of chromatin. However, until now, we have lacked the tools to investigate the relationship between local and global material properties with sufficient resolution. In order to understand the mechanistic basis of local chromatin material state, we sought to determine whether local compaction state is correlated with asymmetric movement. We measured the local chromatin density at telomeres by quantifying

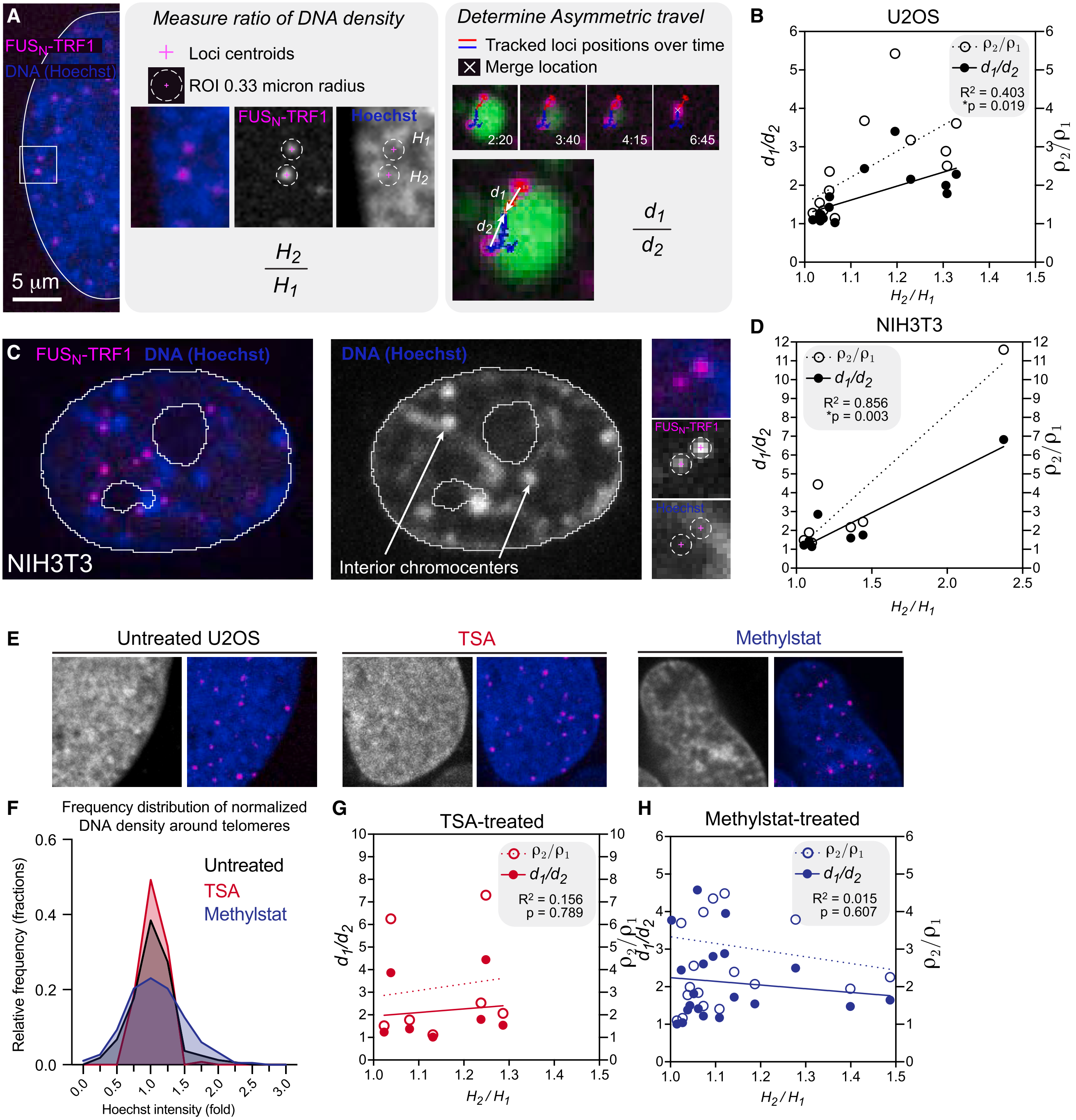

Figure 6. DNA density and epigenetic inhibitors control local chromatin viscoelasticity

(A) Example images and quantification pipeline of Hoechst intensities at target loci in U2OS cells. Ratio of DNA density (H_2/H_1) of the Hoechst channel fluorescent intensities measured within a 0.33 μm radius (2 pixels) of the loci. Asymmetric travel (d_1/d_2) is the ratio of the distance traveled by the first telomere over the distance traveled by the second telomeres.

(B) Graph of Asymmetric travel (d_1/d_2, left axis) or viscoelastic ratio (ρ_2/ρ_1, right axis) vs. ratio of DNA density (H_2/H_1) for telomeres measured with FUS$_N$-TRF1-adhesion module in n = 14 loci pairs from U2OS nuclei.

(C) Example images and Hoechst quantification for NIH3T3 cells. Arrows: interior chromocenters.

(D) Graph of asymmetric travel (d_1/d_2, left axis) or viscoelastic ratio (ρ_2/ρ_1, right axis) vs. Hoechst difference for telomeres in n = 7 loci pairs from NIH3T3 nuclei.

(E) Example images demonstrating DNA density by Hoechst intensity in untreated (left), TSA-treated (center), and methylstat-treated (right) U2OS cell nuclei.

(legend continued on next page)

Hoechst-labeled intensity in a 0.33 μm radius around each telomere locus labeled with FUS_N-miRFP670-TRF1 (Figure 6A). We find that the ratio of chromatin density in telomeric pairs is correlated with their asymmetric movement and therefore differential viscoelasticity (Figure 6B, $R^2 = 0.403$, $^*p = 0.019$). This intensity correlation holds true in mouse fibroblast NIH3T3 cells, whose DNA-dense heterochromatic domains, or chromocenters, are found internally as well as peripherally (Figures 6C and 6D), suggesting that DNA density is correlated with local viscoelasticity, independent of nuclear position.

Global nuclear mechanics can be altered with small molecule drugs that affect epigenetic modifying enzymes, including trichostatin A (TSA), a histone deacetylase inhibitor that increases acetylation and reduces variation in chromatin density across the nucleus,[53] and methylstat, a histone demethylase inhibitor that increases methylation and increases variation in chromatin density.[53] These treatments lead to the expected DNA distributions in U2OS cells (Figures 6E and 6F), and telomeres are found throughout these differentially compacted regions (Figures S6A–S6C). MSD of tracked telomeres in TSA-treated U2OS cells shows that they diffuse with a higher exponent ($\alpha = 0.6678$) than untreated cells ($\alpha = 0.6227$), while telomeres in methylstat-treated cells exhibit a lower diffusive exponent ($\alpha = 0.4685$) (Figures S6D–S6F), consistent with previous reports.[53,65] After calibrating the Rouse polymer-based force estimation model on these MSD data, we confirm that FUS_N condensates apply the same 0.2–1 pN range of force in each condition (Figure S6G). We find that these epigenetic inhibitors decouple movement asymmetry and viscoelasticity from local DNA density in TSA- and methylstat-treated cells (Figures 6G and 6H), suggesting that DNA density is not the only determinant of local viscoelastic state and that averaged measurements like MSD miss important local variations in mechanics.

Taken together, though the number of loci measured under these perturbations is not extensive, the data point to a mechanism in which local mechanical heterogeneity of chromatin arises from a combination of compaction state and epigenetic modifications. The lack of direct correlation between local and global mechanical states is an engaging concept that will undoubtedly be the subject of future studies.

DISCUSSION

In this work, we developed VECTOR, a technique that deploys synthetic light-controlled condensates to impart force on specific chromatin loci in living cells and consequently reposition them. Using VECTOR, we showed how biomolecular condensates generate pN-level forces and harnessed these forces to characterize material responses across nuclear positions. Our findings on (1) lack of significant correlation between degree of displacement (strain) and detachment probability, (2) velocity rate-dependence of detachment probability, and (3) high frequency of incomplete locus recoil suggest that the material state of chromatin at the mesoscale is consistent with a viscoelastic fluid. Together with locus MSD data, these findings are generally consistent with predictions of a Rouse polymer. However, chromatin exhibits heterogeneity in viscoelastic resistance, coupled to nuclear position. Our findings demonstrate the utility of condensate capillarity in applying precise forces onto subcellular targets and underscore the complexity and heterogeneity of the viscoelastic chromatin material state within the nucleus (Figure 7).

VECTOR demonstrates that condensates can generate appreciable interfacial forces up to the pN-level, a magnitude comparable to ATP-fueled molecular motors, though in this case the energy is stored in condensate interfaces. Light deactivation shrinks the loci-spanning condensate, dictating the rate of loci movement, which we find to be between 0.75 and 1.25 μm/min. This speed is comparable to whole-chromosome movement in mitosis but not as rapid as individual molecular motors such as kinesin, which walk along microtubules (MTs) at 2–3 μm/s.[66] Work is generated by dissolving condensates, reminiscent of force generation through disassembling MTs.[67] Sustained attachment to the object against which force is applied is key (e.g., Dam1 in the case of MTs,[67] IDR-mediated adhesion in VECTOR).

VECTOR harnesses and directs these interfacial forces via IDR-mediated adhesion between the condensate and targeted telomeric or non-telomeric repetitive loci, which are efficient nucleation seeds for synthetic condensates.[23,43] Regulated assembly and disassembly of endogenous chromatin-interacting condensates like transcription factor hubs,[68,69] which form and dissolve on the order of minutes, may represent an additional layer of spatiotemporal regulation of pairwise locus interactions related to mammalian gene expression. Long-lived nuclear bodies like nuclear speckles, histone locus bodies, and Cajal bodies may also shape the 3D genomic landscape and transcriptional activity, serving as anchor points for adhesion of linearly distant loci and explaining long-range and inter-chromosomal interactions observed using chromatin conformation capture techniques.[33,70,71] We showed that VECTOR can also reposition non-chromatin nuclear bodies, namely Cajal bodies (Figures S2E–S2G), suggesting that a variety of cellular structures may be targeted by condensate-generated forces. Further adaptations of VECTOR could enable examination of the nature of pairwise locus interactions, locus positioning relative to nuclear bodies/compartments,[34,72] and kinetics of associated functional outcomes.

Adhesion between chromatin-bound, self-interacting proteins like TRF1 can counteract a locus' tendency to recoil upon repositioning, suggesting that chromatin-bound IDRs mediate stable long-distance or interchromosomal genomic interactions as observed with telomere clustering, heterochromatic domain coalescence, and even certain enhancer-promoter contacts.[52]

(F) Frequency distribution of normalized DNA density in a 0.33 μm radius ROI around telomeres; untreated $N = 164$ loci from 13 nuclei; TSA $N = 130$ loci from 9 nuclei; methylstat = 182 loci from 20 nuclei.

(G and H) Graph of asymmetric travel (d_1/d_2, left axis) or viscoelastic ratio (ρ_2/ρ_1, right axis) vs. Hoechst difference for $n = 7$ telomere pairs in TSA-treated (G) or $n = 20$ loci pairs in methylstat-treated (H) U2OS nuclei. Trends are not significant in TSA- or methylstat-treated correlations.

See also Figure S6.

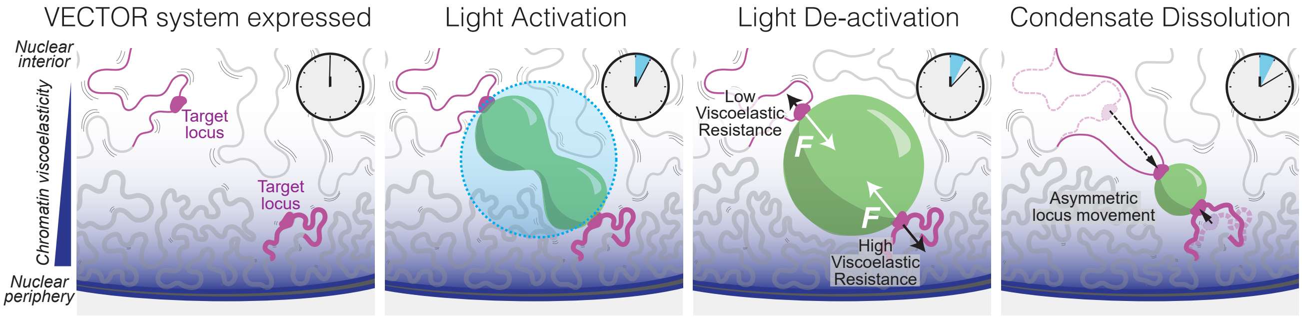

Engineered ‘sticky’ target loci

Chromatin-tethered condensate formation

Force applied to target loci

Chromatin locus repositioning

Figure 7. Interfacial interactions mediate precise force generation in living cells

Target chromatin loci are bound by VECTOR system proteins, creating seeding sites for light-inducible condensates to grow and fuse during a few minutes of localized blue light activation. Upon light deactivation, target loci remain attached to the shrinking condensate due to interfacial interactions, leading to equal forces applied on the attached loci. Uneven viscoelastic resistance of the attached loci leads to asymmetric repositioning events, revealing increased local chromatin viscoelasticity near the nuclear periphery.

Endogenous levels of shelterin proteins (including TRF1) poorly mediate this long-term self-interaction between repositioned telomeres, while non-stoichiometric overexpression of TRF1 does, suggesting that while miscibility of telomeric DNA regions[40] is sufficient for fusion of proximal telomeres, it is not sufficient to counteract the restoring force of the chromatin network. Potentially, imbalanced stoichiometry due to TRF1 overexpression results in increased strength of telomere associations that prevent recoil in our synthetic clustering system and lead to aberrant telomere clustering and formation of dicentric chromosome bridges in previous studies.[50,51] Future studies will unravel differences between cases where long-distance locus associations are functional,[73,74] as with enhancer-promoter interactions, and dysfunctional as with telomere bridges.

Chromatin loci experiencing forces via VECTOR show force-response and recoil behavior consistent with a viscoelastic liquid. Previously, the discrepancy between lack of intermixing of chromatin with itself (e.g., labeled histones or replication-labeled DNA) and rapid fluorescence recovery after photobleaching (FRAP) recovery of chromatin-binding proteins (e.g., heterochromatic factors) have been interpreted as a solid-like chromatin scaffold surrounded by a nucleoplasmic liquid.[27,28] However, here we have directly measured chromatin mechanics with VECTOR as an active rheology tool, illustrating that at the mesoscale (~1 μm), chromatin has both viscous and elastic components. We find that loci recoil incompletely, indicating a partially dissipative viscoelastic liquid rather than a purely elastic solid model of chromatin. Our active rheological measurements can be explained equally well by a phenomenological spring-dashpot Jeffreys viscoelastic liquid model or Rouse polymer model, but the Rouse model is more consistent with all data, including the observed slope of $\alpha \sim 0.5$ in MSD. A viscoelastic liquid model arising from Rouse-like chromatin polymer movement is consistent with previous work, including constrained and coordinated diffusion of chromatin[75,76] and scale-dependent protein mobility within the chromatin environment.[77,78]

Importantly, we measured mechanical heterogeneity within the nucleus up to 3-fold higher near nuclear and nucleolar peripheries than in the interior, which is consistent with known subnuclear localization of heterochromatin.[79] Increased chromatin compaction of heterochromatic sequences[80] correlate with asymmetric locus repositioning in both U2OS and NIH3T3 cell types, and increased rigidity at the nuclear periphery would explain observations of high mechanical stiffness of the whole nucleus,[53,81] even while interior genomic elements exhibit more fluid-like viscoelastic response. Interestingly, recoil behaviors of a chromosomal-internal locus (PPP1R2) do not differ from those of end loci (telomeres), suggesting that linear chromosomal positioning is not a strong predictor of viscoelasticity. Our results highlight the complex relationship between local and global mechanics within the nucleus and underscore contributions of nuclear positioning, chromatin compaction, and epigenetic alterations to nuclear organization and function.

In this work, we have deployed synthetic biomolecular condensates for systematic and programmable generation of intracellular forces and used these forces to interrogate mechanical properties of the genome. We have described the utility of capillary forces and interfacial adhesion between condensates and cellular objects to do organizational work within living cells and suggest that endogenous condensates may utilize their interfacial interactions for similar purposes. Our results underscore the ubiquitous nature of such intracellular interfacial forces and their potential importance in regulating physical changes of the 3D genome and other structures.[37] The interplay between forces generated by condensates and the mechanical resistance of cellular structures provides an exciting perspective on the rich regulatory landscape underlying chromatin compartmentalization, nuclear organization, and their consequences for cellular physiology and disease.

Limitations of the study

VECTOR is limited by several aspects of the light-induced condensates for force application: the total distance a locus can be moved is set by the achievable diameter of the condensate, and the velocity at which it moves is set by the condensate’s dissolution rate. Using the dCas9-based adhesion module of

VECTOR, we can reposition repetitive PPP1R2 and telomeres, though this large number of bound proteins could alter the endogenous material state of the locus, and repositioning of non-repetitive loci will require further methodological development. For future applications of the dCas9 adhesion module to unique loci, a tiled array of 30–100 guides may still efficiently label loci,[82] though the lower limit of number of chromatin-binding sites required to transmit force to the chromatin is currently unknown. Our simulations accurately predict the relative mechanical stiffness difference between two loci, but the reported force values are estimates. With VECTOR, we can compare mechanical measurements of chromatin loci across nuclear positions with high spatial resolution; however, future studies are needed to determine whether rapid movement of a locus is sufficient to induce changes in gene expression and nuclear function.

STAR★METHODS

Detailed methods are provided in the online version of this paper and include the following:

- KEY RESOURCES TABLE
- RESOURCE AVAILABILITY
  - Lead contact
  - Materials availability
  - Data and code availability
- EXPERIMENTAL MODEL AND STUDY PARTICIPANT DETAILS
  - Cell culture
  - Construct design and cloning
  - Lentivirus production and lentiviral transduction
  - Cell culture small molecule inhibitor treatment
  - Optimization for dCas9-based adhesion module
- METHOD DETAILS
  - Microscopy
  - Optogenetic stimulation
  - Automated imaging protocol
  - Limitations of preceding automated activation protocols
  - Physical model
- QUANTIFICATION AND STATISTICAL ANALYSIS
  - Kymograph production
  - Loci tracking during repositioning
  - Detachment probability
  - Estimating number of IDR-IDR interactions at the chromatin-condensate interface
  - Detachment probability as a function of strain and velocity
  - Symmetric/asymmetric locus movement characterization
  - Heterogeneity in chromatin viscoelasticity
  - Hoechst intensity analysis
  - Mean squared displacement analyses
  - Passive microrheology to determine viscoelastic moduli
  - Initial order of magnitude force estimation from telomere trajectories
  - Generating pull-force estimation plots
  - Statistical analysis

SUPPLEMENTAL INFORMATION

Supplemental information can be found online at https://doi.org/10.1016/j.cell.2024.07.034.

ACKNOWLEDGMENTS

We thank Leonid Mirny, Antoine Coulon, Simon Grosse-Holz, and Veer Keizer for helpful discussions regarding estimating pull force applied on chromatin loci and for sharing their "Rousepull" code (https://github.com/OpenTrajectoryAnalysis/rousepull); Mikko Haataja for helpful advice on the modeling, Shunsuke Shimobayashi for the FUS_N-miRFP670-TRF1 and HNRNPA1_C-miRFP670-TRF1 constructs; Mackenzie Walls for the FUS_N mutant original vectors; David Sanders for the FM5 vectors; Jing Xia for the array patterning protocol; Jessica Zhao for sharing code for MSD analysis; Lennard Wiesner for thoughtful comments on the manuscript; Evangelos Gatzogiannis for microscopy assistance; and other members of the Brangwynne Lab for helpful feedback and discussions.

This work was supported by the Howard Hughes Medical Institute, the Princeton Biomolecular Condensate Program, the Princeton Center for Complex Materials, a MRSEC (NSF DMR-2011750), the St. Jude Collaborative on Membraneless Organelles, and the AFOSR MURI (FA9550-20-1-0241). A.R.S. is a Life Science Research Foundation fellow through the Mark Foundation for Cancer Research (No. AWD1006303) and a K99/R00 Pathway to Independence Fellow (K99CA276886-01). Y.K. was supported by the NSF GRFP (DGE-2039656). H.Z. is supported by the Princeton Bioengineering Institute Innovators (PBI^2) Postdoctoral Fellowship.

AUTHOR CONTRIBUTIONS

A.R.S., Y.K., and C.P.B. designed the study. A.R.S. and Y.K. performed experiments and analysis with advice from C.S., H.Z., and C.P.B. H.Z. created experiment-parallel simulations with advice from A.K. Y.-C.C. developed original technologies that provided the basis for these experiments, developed the dCas9-based VECTOR platform, and performed dCas9-based VECTOR experiments. N.D.O. performed telomere MSD tracking and pairwise data analysis. A.R.S., Y.K., and C.P.B. wrote the manuscript, and A.R.S. and Y.K. made the figures with contributions from all authors.

DECLARATION OF INTERESTS

C.P.B. is a scientific founder, Scientific Advisory Board member, shareholder, and consultant for Nereid Therapeutics.

Received: February 27, 2023
Revised: April 22, 2024
Accepted: July 19, 2024
Published: August 20, 2024

REFERENCES

1. Shin, Y., and Brangwynne, C.P. (2017). Liquid phase condensation in cell physiology and disease. Science *357*, eaaf4382. https://doi.org/10.1126/science.aaf4382.
2. Nott, T.J., Petsalaki, E., Farber, P., Jervis, D., Fussner, E., Plochowietz, A., Craggs, T.D., Bazett-Jones, D.P., Pawson, T., Forman-Kay, J.D., et al. (2015). Phase transition of a disordered nuage protein generates environmentally responsive membraneless organelles. Mol. Cell *57*, 936–947. https://doi.org/10.1016/j.molcel.2015.01.013.
3. Brangwynne, C.P., Eckmann, C.R., Courson, D.S., Rybarska, A., Hoege, C., Gharakhani, J., Jülicher, F., and Hyman, A.A. (2009). Germline P granules are liquid droplets that localize by controlled dissolution/condensation. Science *324*, 1729–1732. https://doi.org/10.1126/science.1172046.
4. Su, X., Ditlev, J.A., Hui, E., Xing, W., Banjade, S., Okrut, J., King, D.S., Taunton, J., Rosen, M.K., and Vale, R.D. (2016). Phase separation of signaling molecules promotes T cell receptor signal transduction. Science *352*, 595–599. https://doi.org/10.1126/science.aad9964.
5. Molliex, A., Temirov, J., Lee, J., Coughlin, M., Kanagaraj, A.P., Kim, H.J., Mittag, T., and Taylor, J.P. (2015). Phase separation by low complexity domains promotes stress granule assembly and drives pathological fibrillization. Cell *163*, 123–133. https://doi.org/10.1016/j.cell.2015.09.015.
6. Freeman Rosenzweig, E.S., Xu, B., Kuhn Cuellar, L., Martinez-Sanchez, A., Schaffer, M., Strauss, M., Cartwright, H.N., Ronceray, P., Plitzko,

J.M., Förster, F., et al. (2017). The Eukaryotic CO2-Concentrating Organelle Is Liquid-like and Exhibits Dynamic Reorganization. Cell *171*, 148–162.e19. https://doi.org/10.1016/j.cell.2017.08.008.

7. Feric, M., Vaidya, N., Harmon, T.S., Mitrea, D.M., Zhu, L., Richardson, T.M., Kriwacki, R.W., Pappu, R.V., and Brangwynne, C.P. (2016). Coexisting Liquid Phases Underlie Nucleolar Subcompartments. Cell *165*, 1686–1697. https://doi.org/10.1016/j.cell.2016.04.047.
8. Patil, A., Strom, A.R., Paulo, J.A., Collings, C.K., Ruff, K.M., Shinn, M.K., Sankar, A., Cervantes, K.S., Wauer, T., St Laurent, J.D., et al. (2023). A disordered region controls cBAF activity via condensation and partner recruitment. Cell *186*, 4936–4955.e26. https://doi.org/10.1016/j.cell.2023.08.032.
9. Hnisz, D., Shrinivas, K., Young, R.A., Chakraborty, A.K., and Sharp, P.A. (2017). A Phase Separation Model for Transcriptional Control. Cell *169*, 13–23. https://doi.org/10.1016/j.cell.2017.02.007.
10. Plys, A.J., and Kingston, R.E. (2018). Dynamic condensates activate transcription. Science *361*, 329–330. https://doi.org/10.1126/science.aau4795.
11. Treen, N., Shimobayashi, S.F., Eeftens, J., Brangwynne, C.P., and Levine, M. (2021). Properties of repression condensates in living Ciona embryos. Nat. Commun. *12*, 1561. https://doi.org/10.1038/s41467-021-21606-5.
12. Strom, A.R., Emelyanov, A.V., Mir, M., Fyodorov, D.V., Darzacq, X., and Karpen, G.H. (2017). Phase separation drives heterochromatin domain formation. Nature *547*, 241–245. https://doi.org/10.1038/nature22989.
13. Larson, A.G., Elnatan, D., Keenen, M.M., Trnka, M.J., Johnston, J.B., Burlingame, A.L., Agard, D.A., Redding, S., and Narlikar, G.J. (2017). Liquid droplet formation by HP1α suggests a role for phase separation in heterochromatin. Nature *547*, 236–240. https://doi.org/10.1038/nature22822.
14. Falk, M., Feodorova, Y., Naumova, N., Imakaev, M., Lajoie, B.R., Leonhardt, H., Joffe, B., Dekker, J., Fudenberg, G., Solovei, I., et al. (2019). Heterochromatin drives compartmentalization of inverted and conventional nuclei. Nature *570*, 395–399. https://doi.org/10.1038/s41586-019-1275-3.
15. Chakraborty, A., and Ay, F. (2019). The role of 3D genome organization in disease: from compartments to single nucleotides. Semin. Cell Dev. Biol. *90*, 104–113. https://doi.org/10.1016/j.semcdb.2018.07.005.
16. Boija, A., Klein, I.A., and Young, R.A. (2021). Biomolecular Condensates and Cancer. Cancer Cell *39*, 174–192. https://doi.org/10.1016/j.ccell.2020.12.003.
17. Rosowski, K.A., Sai, T., Vidal-Henriquez, E., Zwicker, D., Style, R.W., and Dufresne, E.R. (2020). Elastic ripening and inhibition of liquid–liquid phase separation. Nat. Phys. *16*, 422–425. https://doi.org/10.1038/s41567-019-0767-2.
18. Vidal-Henriquez, E., and Zwicker, D. (2020). Theory of droplet ripening in stiffness gradients. Soft Matter *16*, 5898–5905. https://doi.org/10.1039/d0sm00182a.
19. Böddeker, T.J., Rosowski, K.A., Berchtold, D., Emmanouilidis, L., Han, Y., Allain, F.H.T., Style, R.W., Pelkmans, L., and Dufresne, E.R. (2022). Non-specific adhesive forces between filaments and membraneless organelles. Nat. Phys. *18*, 571–578. https://doi.org/10.1038/s41567-022-01537-8.
20. Wiegand, T., and Hyman, A.A. (2020). Drops and fibers - how biomolecular condensates and cytoskeletal filaments influence each other. Emerg. Top. Life Sci. *4*, 247–261. https://doi.org/10.1042/ETLS20190174.
21. Lee, D.S.W., Strom, A.R., and Brangwynne, C.P. (2022). The mechanobiology of nuclear phase separation. APL Bioeng. *6*, 021503. https://doi.org/10.1063/5.0083286.
22. Feric, M., and Brangwynne, C.P. (2013). A nuclear F-actin scaffold stabilizes ribonucleoprotein droplets against gravity in large cells. Nat. Cell Biol. *15*, 1253–1259. https://doi.org/10.1038/ncb2830.
23. Shin, Y., Chang, Y.-C., Lee, D.S.W., Berry, J., Sanders, D.W., Ronceray, P., Wingreen, N.S., Haataja, M., and Brangwynne, C.P. (2018). Liquid Nuclear Condensates Mechanically Sense and Restructure the Genome. Cell *175*, 1481–1491.e13. https://doi.org/10.1016/j.cell.2018.10.057.
24. Lee, D.S.W., Wingreen, N.S., and Brangwynne, C.P. (2021). Chromatin mechanics dictates subdiffusion and coarsening dynamics of embedded condensates. Nat. Phys. *17*, 531–538. https://doi.org/10.1038/s41567-020-01125-8.
25. Caragine, C.M., Haley, S.C., and Zidovska, A. (2019). Nucleolar dynamics and interactions with nucleoplasm in living cells. eLife *8*, e47533. https://doi.org/10.7554/eLife.47533.
26. Zidovska, A. (2020). The rich inner life of the cell nucleus: dynamic organization, active flows, and emergent rheology. Biophys. Rev. *12*, 1093–1106. https://doi.org/10.1007/s12551-020-00761-x.
27. Strickfaden, H., Tolsma, T.O., Sharma, A., Underhill, D.A., Hansen, J.C., and Hendzel, M.J. (2020). Condensed Chromatin Behaves like a Solid on the Mesoscale In Vitro and in Living Cells. Cell *183*, 1772–1784.e13. https://doi.org/10.1016/j.cell.2020.11.027.
28. de Vries, A.H.B., Krenn, B.E., van Driel, R., Subramaniam, V., and Kanger, J.S. (2007). Direct observation of nanomechanical properties of chromatin in living cells. Nano Lett. *7*, 1424–1427. https://doi.org/10.1021/nl070603+.
29. Dubochet, J., Adrian, M., Schultz, P., and Oudet, P. (1986). Cryo-electron microscopy of vitrified SV40 minichromosomes: the liquid drop model. EMBO J. *5*, 519–528. https://doi.org/10.1002/j.1460-2075.1986.tb04241.x.
30. Keizer, V.I.P., Grosse-Holz, S., Woringer, M., Zambon, L., Aizel, K., Bongaerts, M., Delille, F., Kolar-Znika, L., Scolari, V.F., Hoffmann, S., et al. (2022). Live-cell micromanipulation of a genomic locus reveals interphase chromatin mechanics. Science *377*, 489–495. https://doi.org/10.1126/science.abi9810.
31. Therizols, P., Illingworth, R.S., Courilleau, C., Boyle, S., Wood, A.J., and Bickmore, W.A. (2014). Chromatin decondensation is sufficient to alter nuclear organization in embryonic stem cells. Science *346*, 1238–1242. https://doi.org/10.1126/science.1259587.
32. Harewood, L., Schütz, F., Boyle, S., Perry, P., Delorenzi, M., Bickmore, W.A., and Reymond, A. (2010). The effect of translocation-induced nuclear reorganization on gene expression. Genome Res. *20*, 554–564. https://doi.org/10.1101/gr.103622.109.
33. Pindyurin, A.V., and Fishman, V. (2022). Editorial: The Role of High-Order Chromatin Organization in Gene Regulation. Front. Genet. *13*, 1045787.
34. Wang, H., Xu, X., Nguyen, C.M., Liu, Y., Gao, Y., Lin, X., Daley, T., Kipniss, N.H., La Russa, M., and Qi, L.S. (2018). CRISPR-Mediated Programmable 3D Genome Positioning and Nuclear Organization. Cell *175*, 1405–1417.e14. https://doi.org/10.1016/j.cell.2018.09.013.
35. Kumaran, R.I., Thakar, R., and Spector, D.L. (2008). Chromatin dynamics and gene positioning. Cell *132*, 929–934. https://doi.org/10.1016/j.cell.2008.03.004.
36. Kumaran, R.I., and Spector, D.L. (2008). A genetic locus targeted to the nuclear periphery in living cells maintains its transcriptional competence. J. Cell Biol. *180*, 51–65. https://doi.org/10.1083/jcb.200706060.
37. Gouveia, B., Kim, Y., Shaevitz, J.W., Petry, S., Stone, H.A., and Brangwynne, C.P. (2022). Capillary forces generated by biomolecular condensates. Nature *609*, 255–264. https://doi.org/10.1038/s41586-022-05138-6.
38. Setru, S.U., Gouveia, B., Alfaro-Aco, R., Shaevitz, J.W., Stone, H.A., and Petry, S. (2021). A hydrodynamic instability drives protein droplet formation on microtubules to nucleate branches. Nat. Phys. *17*, 493–498. https://doi.org/10.1038/s41567-020-01141-8.
39. Folkmann, A.W., Putnam, A., Lee, C.F., and Seydoux, G. (2021). Regulation of biomolecular condensates by interfacial protein clusters. Science *373*, 1218–1224. https://doi.org/10.1126/science.abg7071.

40. Jack, A., Kim, Y., Strom, A.R., Lee, D.S.W., Williams, B., Schaub, J.M., Kellogg, E.H., Finkelstein, I.J., Ferro, L.S., Yildiz, A., et al. (2022). Compartmentalization of telomeres through DNA-scaffolded phase separation. Dev. Cell *57*, 277–290.e9. https://doi.org/10.1016/j.devcel.2021.12.017.
41. Bergeron-Sandoval, L.-P., Kumar, S., Heris, H.K., Chang, C.L.A., Cornell, C.E., Keller, S.L., François, P., Hendricks, A.G., Ehrlicher, A.J., Pappu, R.V., et al. (2021). Endocytic proteins with prion-like domains form viscoelastic condensates that enable membrane remodeling. Proc. Natl. Acad. Sci. USA *118*, e2113789118. https://doi.org/10.1073/pnas.2113789118.
42. Bracha, D., Walls, M.T., Wei, M.-T., Zhu, L., Kurian, M., Avalos, J.L., Toettcher, J.E., and Brangwynne, C.P. (2018). Mapping Local and Global Liquid Phase Behavior in Living Cells Using Photo-Oligomerizable Seeds. Cell *175*, 1467. https://doi.org/10.1016/j.cell.2018.10.048.
43. Shimobayashi, S.F., Ronceray, P., Sanders, D.W., Haataja, M.P., and Brangwynne, C.P. (2021). Nucleation landscape of biomolecular condensates. Nature *599*, 503–506. https://doi.org/10.1038/s41586-021-03905-5.
44. Wang, H., Kelley, F.M., Milovanovic, D., Schuster, B.S., and Shi, Z. (2021). Surface tension and viscosity of protein condensates quantified by micropipette aspiration. Biophys. Rep. (N Y) *1*, 100011. https://doi.org/10.1016/j.bpr.2021.100011.
45. Jawerth, L.M., Ijavi, M., Ruer, M., Saha, S., Jahnel, M., Hyman, A.A., Jülicher, F., and Fischer-Friedrich, E. (2018). Salt-Dependent Rheology and Surface Tension of Protein Condensates Using Optical Traps. Phys. Rev. Lett. *121*, 258101. https://doi.org/10.1103/PhysRevLett.121.258101.
46. Kato, M., Han, T.W., Xie, S., Shi, K., Du, X., Wu, L.C., Mirzaei, H., Goldsmith, E.J., Longgood, J., Pei, J., et al. (2012). Cell-free formation of RNA granules: low complexity sequence domains form dynamic fibers within hydrogels. Cell *149*, 753–767. https://doi.org/10.1016/j.cell.2012.04.017.
47. Wang, J., Choi, J.-M., Holehouse, A.S., Lee, H.O., Zhang, X., Jahnel, M., Maharana, S., Lemaitre, R., Pozniakovsky, A., Drechsel, D., et al. (2018). A Molecular Grammar Governing the Driving Forces for Phase Separation of Prion-like RNA Binding Proteins. Cell *174*, 688–699.e16. https://doi.org/10.1016/j.cell.2018.06.006.
48. Protter, D.S.W., Rao, B.S., Van Treeck, B., Lin, Y., Mizoue, L., Rosen, M.K., and Parker, R. (2018). Intrinsically Disordered Regions Can Contribute Promiscuous Interactions to RNP Granule Assembly. Cell Rep. *22*, 1401–1412. https://doi.org/10.1016/j.celrep.2018.01.036.
49. Martin, E.W., Holehouse, A.S., Peran, I., Farag, M., Incicco, J.J., Bremer, A., Grace, C.R., Soranno, A., Pappu, R.V., and Mittag, T. (2020). Valence and patterning of aromatic residues determine the phase behavior of prion-like domains. Science *367*, 694–699. https://doi.org/10.1126/science.aaw8653.
50. Lisaingo, K., Uringa, E.-J., and Lansdorp, P.M. (2014). Resolution of telomere associations by TRF1 cleavage in mouse embryonic stem cells. Mol. Biol. Cell *25*, 1958–1968. https://doi.org/10.1091/mbc.E13-10-0564.
51. Nera, B., Huang, H.-S., Lai, T., and Xu, L. (2015). Elevated levels of TRF2 induce telomeric ultrafine anaphase bridges and rapid telomere deletions. Nat. Commun. *6*, 10132. https://doi.org/10.1038/ncomms10132.
52. Ahn, J.H., Davis, E.S., Daugird, T.A., Zhao, S., Quiroga, I.Y., Uryu, H., Li, J., Storey, A.J., Tsai, Y.-H., Keeley, D.P., et al. (2021). Phase separation drives aberrant chromatin looping and cancer development. Nature *595*, 591–595. https://doi.org/10.1038/s41586-021-03662-5.
53. Stephens, A.D., Banigan, E.J., Adam, S.A., Goldman, R.D., and Marko, J.F. (2017). Chromatin and lamin A determine two different mechanical response regimes of the cell nucleus. Mol. Biol. Cell *28*, 1984–1996. https://doi.org/10.1091/mbc.E16-09-0653.
54. Hobson, C., Nelsen, E.F., Hsiao, J., Stephens, A., Timothy O'Brien, E., Falvo, M.R., and Superfine, R. (2019). Nuclear Deformation with Combined AFM and 3D Multi-Color Live-Cell Line Bessel Sheet Imaging. Biophys. J. *116*, 24a. https://doi.org/10.1016/j.bpj.2018.11.173.
55. Rubinstein, M., and Colby, R.H. (2003). Polymer Physics (Oxford University Press).
56. Zhou, H.-X. (2021). Viscoelasticity of biomolecular condensates conforms to the Jeffreys model. J. Chem. Phys. *154*, 041103. https://doi.org/10.1063/5.0038916.
57. Rouse, P.E. (1953). A theory of the linear viscoelastic properties of dilute solutions of coiling polymers. J. Chem. Phys. *21*, 1272–1280. https://doi.org/10.1063/1.1699180.
58. Ferry, J.D., Landel, R.F., and Williams, M.L. (1955). Extensions of the Rouse theory of viscoelastic properties to undiluted linear polymers. J. Appl. Phys. *26*, 359–362. https://doi.org/10.1063/1.1721997.
59. Vandebroek, H., and Vanderzande, C. (2015). Dynamics of a polymer in an active and viscoelastic bath. Phys. Rev. E Stat. Nonlin. Soft Matter Phys. *92*, 060601. https://doi.org/10.1103/PhysRevE.92.060601.
60. Hertzog, M., and Erdel, F. (2023). The Material Properties of the Cell Nucleus: A Matter of Scale. Cells *12*. https://doi.org/10.3390/cells12151958.
61. Howard, J. (2005). Mechanics of Motor Proteins and the Cytoskeleton (Sinauer).
62. Bronshtein, I., Kepten, E., Kanter, I., Berezin, S., Lindner, M., Redwood, A.B., Mai, S., Gonzalo, S., Foisner, R., Shav-Tal, Y., et al. (2015). Loss of lamin A function increases chromatin dynamics in the nuclear interior. Nat. Commun. *6*, 8044. https://doi.org/10.1038/ncomms9044.
63. Bizhanova, A., and Kaufman, P.D. (2021). Close to the edge: Heterochromatin at the nucleolar and nuclear peripheries. Biochim. Biophys. Acta Gene Regul. Mech. *1864*, 194666. https://doi.org/10.1016/j.bbagrm.2020.194666.
64. Chubb, J.R., Boyle, S., Perry, P., and Bickmore, W.A. (2002). Chromatin motion is constrained by association with nuclear compartments in human cells. Curr. Biol. *12*, 439–445. https://doi.org/10.1016/s0960-9822(02)00695-4.
65. Strom, A.R., Biggs, R.J., Banigan, E.J., Wang, X., Chiu, K., Herman, C., Collado, J., Yue, F., Ritland Politz, J.C., Tait, L.J., et al. (2021). HP1α is a chromatin crosslinker that controls nuclear and mitotic chromosome mechanics. eLife *10*, e63972. https://doi.org/10.7554/eLife.63972.
66. Alberts, B., Johnson, A., Lewis, J., Raff, M., Roberts, K., and Walter, P. (2002). Molecular Biology of the Cell (Garland Science).
67. Asbury, C.L., Gestaut, D.R., Powers, A.F., Franck, A.D., and Davis, T.N. (2006). The Dam1 kinetochore complex harnesses microtubule dynamics to produce force and movement. Proc. Natl. Acad. Sci. USA *103*, 9873–9878. https://doi.org/10.1073/pnas.0602249103.
68. Sabari, B.R., Dall'Agnese, A., Boija, A., Klein, I.A., Coffey, E.L., Shrinivas, K., Abraham, B.J., Hannett, N.M., Zamudio, A.V., Manteiga, J.C., et al. (2018). Coactivator condensation at super-enhancers links phase separation and gene control. Science *361*, eaar3958. https://doi.org/10.1126/science.aar3958.
69. Palacio, M., and Taatjes, D.J. (2022). Merging Established Mechanisms with New Insights: Condensates, Hubs, and the Regulation of RNA Polymerase II Transcription. J. Mol. Biol. *434*, 167216. https://doi.org/10.1016/j.jmb.2021.167216.
70. Lu, L., Liu, X., Huang, W.-K., Giusti-Rodríguez, P., Cui, J., Zhang, S., Xu, W., Wen, Z., Ma, S., Rosen, J.D., et al. (2020). Robust Hi-C Maps of Enhancer-Promoter Interactions Reveal the Function of Non-coding Genome in Neural Development and Diseases. Mol. Cell *79*, 521–534.e15. https://doi.org/10.1016/j.molcel.2020.06.007.
71. Ron, G., Globerson, Y., Moran, D., and Kaplan, T. (2017). Promoter-enhancer interactions identified from Hi-C data using probabilistic models and hierarchical topological domains. Nat. Commun. *8*, 2237. https://doi.org/10.1038/s41467-017-02386-3.
72. Quinodoz, S.A., Ollikainen, N., Tabak, B., Palla, A., Schmidt, J.M., Detmar, E., Lai, M.M., Shishkin, A.A., Bhat, P., Takei, Y., et al. (2018).

Higher-Order Inter-chromosomal Hubs Shape 3D Genome Organization in the Nucleus. Cell *174*, 744–757.e24. https://doi.org/10.1016/j.cell.2018.05.024.

73. Feric, M., and Misteli, T. (2021). Phase separation in genome organization across evolution. Trends Cell Biol. *31*, 671–685. https://doi.org/10.1016/j.tcb.2021.03.001.
74. Mazzocca, M., Loffreda, A., Colombo, E., Fillot, T., Gnani, D., Falletta, P., Monteleone, E., Capozi, S., Bertrand, E., Legube, G., et al. (2023). Chromatin organization drives the search mechanism of nuclear factors. Nat. Commun. *14*, 6433. https://doi.org/10.1038/s41467-023-42133-5.
75. Gasser, S.M. (2002). Visualizing chromatin dynamics in interphase nuclei. Science *296*, 1412–1416. https://doi.org/10.1126/science.1067703.
76. Zidovska, A., Weitz, D.A., and Mitchison, T.J. (2013). Micron-scale coherence in interphase chromatin dynamics. Proc. Natl. Acad. Sci. USA *110*, 15555–15560. https://doi.org/10.1073/pnas.1220313110.
77. Erdel, F., Baum, M., and Rippe, K. (2015). The viscoelastic properties of chromatin and the nucleoplasm revealed by scale-dependent protein mobility. J. Phys. Condens. Matter *27*, 064115. https://doi.org/10.1088/0953-8984/27/6/064115.
78. Bancaud, A., Huet, S., Daigle, N., Mozziconacci, J., Beaudouin, J., and Ellenberg, J. (2009). Molecular crowding affects diffusion and binding of nuclear proteins in heterochromatin and reveals the fractal organization of chromatin. EMBO J. *28*, 3785–3798. https://doi.org/10.1038/emboj.2009.340.
79. Reynolds, N., McEvoy, E., Ghosh, S., Panadero Pérez, J.A., Neu, C.P., and McGarry, P. (2021). Image-derived modeling of nucleus strain amplification associated with chromatin heterogeneity. Biophys. J. *120*, 1323–1332. https://doi.org/10.1016/j.bpj.2021.01.040.
80. Heitz, E. (1928). Das heterochromatin der moose (Bornträger).
81. Dupont, S., and Wickström, S.A. (2022). Mechanical regulation of chromatin and transcription. Nat. Rev. Genet. *23*, 624–643. https://doi.org/10.1038/s41576-022-00493-6.
82. Chen, B., Gilbert, L.A., Cimini, B.A., Schnitzbauer, J., Zhang, W., Li, G.-W., Park, J., Blackburn, E.H., Weissman, J.S., Qi, L.S., et al. (2013). Dynamic imaging of genomic loci in living human cells by an optimized CRISPR/Cas system. Cell *155*, 1479–1491. https://doi.org/10.1016/j.cell.2013.12.001.
83. Tanenbaum, M.E., Gilbert, L.A., Qi, L.S., Weissman, J.S., and Vale, R.D. (2014). A protein-tagging system for signal amplification in gene expression and fluorescence imaging. Cell *159*, 635–646. https://doi.org/10.1016/j.cell.2014.09.039.
84. Sanders, D.W., Kedersha, N., Lee, D.S.W., Strom, A.R., Drake, V., Riback, J.A., Bracha, D., Eeftens, J.M., Iwanicki, A., Wang, A., et al. (2020). Competing Protein-RNA Interaction Networks Control Multiphase Intracellular Organization. Cell *181*, 306–324.e28. https://doi.org/10.1016/j.cell.2020.03.050.
85. Schindelin, J., Arganda-Carreras, I., Frise, E., Kaynig, V., Longair, M., Pietzsch, T., Preibisch, S., Rueden, C., Saalfeld, S., Schmid, B., et al. (2012). Fiji: an open-source platform for biological-image analysis. Nat. Methods *9*, 676–682. https://doi.org/10.1038/nmeth.2019.
86. MathWorks, Inc. (2005). MATLAB: the language of technical computing. Desktop tools and development environment, version 7 (MathWorks).
87. Brangwynne, C.P., Tompa, P., and Pappu, R.V. (2015). Polymer physics of intracellular phase transitions. Nat. Phys. *11*, 899–904. https://doi.org/10.1038/nphys3532.
88. Cahn, J.W., and Hilliard, J.E. (1958). Free energy of a nonuniform system. I. interfacial free energy. J. Chem. Phys. *28*, 258–267. https://doi.org/10.1063/1.1744102.
89. Shin, Y., Berry, J., Pannucci, N., Haataja, M.P., Toettcher, J.E., and Brangwynne, C.P. (2017). Spatiotemporal Control of Intracellular Phase Transitions Using Light-Activated optoDroplets. Cell *168*, 159–171.e14. https://doi.org/10.1016/j.cell.2016.11.054.
90. Bray, A.J. (1993). Theory of phase ordering kinetics. Phys. A *194*, 41–52. https://doi.org/10.1016/0378-4371(93)90338-5.
91. Mao, S., Kuldinow, D., Haataja, M.P., and Košmrlj, A. (2019). Phase behavior and morphology of multicomponent liquid mixtures. Soft Matter *15*, 1297–1311. https://doi.org/10.1039/c8sm02045k.
92. Sharma, V. (2018). ImageJ plugin HyperStackReg V5.6. Zenodo. https://doi.org/10.5281/zenodo.2252521.
93. Tinevez, J.-Y., Perry, N., Schindelin, J., Hoopes, G.M., Reynolds, G.D., Laplantine, E., Bednarek, S.Y., Shorte, S.L., and Eliceiri, K.W. (2017). TrackMate: an open and extensible platform for single-particle tracking. Methods *115*, 80–90. https://doi.org/10.1016/j.ymeth.2016.09.016.
94. Doksani, Y., Wu, J.Y., de Lange, T., and Zhuang, X. (2013). Super-resolution fluorescence imaging of telomeres reveals TRF2-dependent T-loop formation. Cell *155*, 345–356. https://doi.org/10.1016/j.cell.2013.09.048.
95. Vancevska, A., Douglass, K.M., Pfeiffer, V., Manley, S., and Lingner, J. (2017). The telomeric DNA damage response occurs in the absence of chromatin decompaction. Genes Dev. *31*, 567–577. https://doi.org/10.1101/gad.294082.116.
96. Bandaria, J.N., Qin, P., Berk, V., Chu, S., and Yildiz, A. (2016). Shelterin Protects Chromosome Ends by Compacting Telomeric Chromatin. Cell *164*, 735–746. https://doi.org/10.1016/j.cell.2016.01.036.
97. Timashev, L.A., Babcock, H., Zhuang, X., and de Lange, T. (2017). The DDR at telomeres lacking intact shelterin does not require substantial chromatin decompaction. Genes Dev. *31*, 578–589. https://doi.org/10.1101/gad.294108.116.
98. Jeynes, J.C.G., Geraki, K., Jeynes, C., Zhaohong, M., Bettiol, A.A., Latorre, E., Harries, L.W., and Soeller, C. (2017). Nanoscale Properties of Human Telomeres Measured with a Dual Purpose X-ray Fluorescence and Super Resolution Microscopy Gold Nanoparticle Probe. ACS Nano *11*, 12632–12640. https://doi.org/10.1021/acsnano.7b07064.
99. Hübner, B., von Otter, E., Ahsan, B., Wee, M.L., Henriksson, S., Ludwig, A., and Sandin, S. (2022). Ultrastructure and nuclear architecture of telomeric chromatin revealed by correlative light and electron microscopy. Nucleic Acids Res. *50*, 5047–5063. https://doi.org/10.1093/nar/gkac309.
100. Mason, T.G. (2000). Estimating the viscoelastic moduli of complex fluids using the generalized Stokes–Einstein equation. Rheol. Acta *39*, 371–378. https://doi.org/10.1007/s003970000094.
101. Smelser, A.M., Macosko, J.C., O'Dell, A.P., Smyre, S., Bonin, K., and Holzwarth, G. (2015). Mechanical properties of normal versus cancerous breast cells. Biomech. Model. Mechanobiol. *14*, 1335–1347. https://doi.org/10.1007/s10237-015-0677-x.
102. Mason, T.G., and Weitz, D.A. (1995). Optical measurements of frequency-dependent linear viscoelastic moduli of complex fluids. Phys. Rev. Lett. *74*, 1250–1253. https://doi.org/10.1103/PhysRevLett.74.1250.

STAR★METHODS

KEY RESOURCES TABLE

REAGENT or RESOURCE	SOURCE	IDENTIFIER
Bacterial and virus strains		
Stellar competent cells	Takara Bio	Cat#636776
Chemicals, peptides, and recombinant proteins		
Trichostatin A (TSA)	Sigma	Cat#T1592
Methylstat	Sigma	Cat#SML0343
Hoechst 33342 solution	Thermo	Cat#62249
GIBCO DMEM, High Glucose, Pyruvate	Thermo	Cat#11995065
GIBCO DPBS, no calcium, no magnesium	Thermo	Cat#14190144
GIBCO Opti-MEM Reduced Serum Medium	Thermo	Cat#31985062
GIBCO Penicillin-Streptomycin (10,000 U/mL)	Thermo	Cat#15140122
Fetal Bovine Serum	Corning	Cat#35-010-CV
Critical commercial assays		
CloneAmp HiFi PCR Premix	Takara Bio	Cat#639298
In-Fusion HD cloning kit	Takara Bio	Cat#638910
Transit293 transfection reagent	Mirus	Cat#MIR2700
Experimental models: Cell lines		
U2OS	ATCC	RRID: CVCL_0042
NIH3T3	ATCC	CLS Cat# 400101, RRID: CVCL_0594
Lenti-X 293T	Takara Bio	Cat#632180
Recombinant DNA		
FUS_N-miRFP670-TRF1	Shimobayashi et al.[43]	N/A
FUS_N^{3YS}-miRFP670-TRF1	This study	N/A
FUS_N^{5YS}-miRFP670-TRF1	Shimobayashi et al.[43]	N/A
FUS_N^{9YS}-miRFP670-TRF1	This study	N/A
FUS_N^{15YS}-miRFP670-TRF1	This study	N/A
FUS_N^{27YS}-miRFP670-TRF1	This study	N/A
$HNRNPA1_C$-miRFP670-TRF1	Shimobayashi et al.[43]	N/A
iLID-miRFP670-TRF1	Jack et al.[40]	N/A
NLS-GFP-iLID-Fe	Bracha et al.[42]	N/A
FUS_N-miRFP670-Coilin	This study	N/A
DDX4-mCherry-SspB	Bracha et al.[42]	N/A
$BRD4^{\Delta N}$-mCherry-SspB	Bracha et al.[42]	N/A
GFP-TRF1	Jack et al.[40]	N/A
GFP-TRF2	Jack et al.[40]	N/A
miRFP670-TRF1	Jack et al.[40]	N/A
dCas9-SunTag(10X)-2A-BFP	Tanenbaum et al.[83]	N/A
$scFv_{(SunTag)}$-HaloTag-iLID	This study	N/A
sgPPPP1R2	This study	N/A
sgTelo[23]	Shin et al.[23]	N/A
Lentiviral helper plasmid PSP	Sanders et al.[84]	N/A
Lentiviral helper plasmid VSVG	Sanders et al.[84]	N/A
Software and algorithms		
Fiji (ImageJ)	Schindelin et al.[85]	https://imagej.net/software/fiji/downloads
MATLAB	MathWorks, Inc.[86]	https://www.mathworks.com/

(Continued on next page)

Continued

REAGENT or RESOURCE	SOURCE	IDENTIFIER
Python 3.7.10	Python Software Foundation	https://python.org
Segmenting nuclear edges	This study	https://zenodo.org/records/12594255
Measuring locus distance from edges	This study	https://zenodo.org/records/12677174
Hoechst analysis	This study	https://zenodo.org/records/12594068
Telomeric viscoelasticity analysis	This study	https://zenodo.org/records/12628456
Simulation code	This study	https://zenodo.org/records/12675332
GraphPad PRISM 9.1.0	GraphPad	https://graphpad.com

RESOURCE AVAILABILITY

Lead contact

Requests for resources and further information should be directed to the lead contact, Cliff Brangwynne (cbrangwy@princeton.edu).

Materials availability

All unique/stable reagents generated in this study are available from the lead contact without restriction. Resources and reagents requests should be directed to the lead contact.

Data and code availability

Raw data reported in this paper will be shared by the lead contact upon request. Original code used to analyze data in this manuscript can be found at the links provided in the key resources table. Any additional information required to reanalyze the data reported herein is available from the lead contact upon request.

EXPERIMENTAL MODEL AND STUDY PARTICIPANT DETAILS

Cell culture

All cell lines were incubated in and grown at 37°C with 5% CO_2. U2OS (human osteosarcoma) and NIH3T3 (mouse fibroblast) cells were obtained from the ATCC (authenticated via ATCC's STR profiling), cultured in DMEM (GIBCO, 11995065) with 10% FBS (Atlanta Biological, S11150H) and 1% streptomycin and penicillin (GIBCO, 15140122), grown at 37°C with 5% CO_2.

Construct design and cloning

FUS_N-miRFP670-TRF1 and $HNRNPA1_C$-miRFP670-TRF1 constructs[43] were generous gifts from Shunsuke Shimobayashi. FUS_N point mutants were PCR-amplified from original vectors[42] gifted by Mackenzie Walls, using CloneAmp HiFi PCR Premix (Takara Bio 639298). These PCR fragments were inserted into linearized FM5 lentiviral vectors that carry standardized linkers that were kind gifts from David Sanders,[84] using the In-Fusion HD cloning kit (Takara Bio, 638910). In addition to these point mutants, all other DNA fragments of interest were cloned using the same protocol and reagents. All constructs were confirmed by GENEWIZ Sanger sequencing.

Lentivirus production and lentiviral transduction

All live cell experiments used cells stably transduced with lentivirus. Lentiviruses were produced by plating Lenti-X 293T cells (Takara Bio, 632180) into 6-well plates to reach ~70% confluence at the time of transfection. 24-48 hours after plating, the transfer plasmid and helper plasmids VSVG and PSP were transfected into the Lenti-X cells using Transit293 transfection reagent (Mirus, MIR 2700) incubated in OptiMEM (modified from Sanders et al.[84]). ~48 hours after transfection, viruses were harvested and filtered using a 0.45 μm filter (Pall Life Sciences) and were either then used immediately or stored at -80°C. U2OS cells plated at 30%–50% confluency in 96-well glass-bottom plates (Cellvis) were transduced for 2-3 days before live-cell imaging experiments.

Cell culture small molecule inhibitor treatment

U2OS cells already transduced with fluorescent constructs were plated on 96-well glass bottom plates and treated with 100 nM Trichostatin A in DMEM for 16-24 hours, or 1 μM methylstat for 48 hours before imaging.

Optimization for dCas9-based adhesion module

U2OS cells were transduced with lentivirus for dCas9-SunTag(10X)-2A-BFP at low multiplicity of infection (MOI), expanded, followed by single-cell sorting. Individual clones were expanded and a portion of each clone was further transduced with lentivirus for scFv-HaloTag-iLID at low MOI and sgTelomere at high MOI for microscopy-based screening. dCas9-expressing clones with clear telomere labeling upon JF646 HaloTag-ligand conjugation were selected and saved for dCas9-based VECTOR experiments.

METHOD DETAILS

Microscopy

Cells for all live cell imaging experiments were plated on 96-well glass-bottom plates and incubated at 37°C and 5% CO_2 by an Okolab microscope stage incubator with a 96-well insert. Images were taken on a spinning disk (Yokogawa CSU-X1) confocal microscope with an Andor DU-897 EMCCD camera on a Nikon Eclipse Ti body and a 100x oil immersion Apo TIRF objective (NA 1.49 MRD01991), and a Nikon LU-NV laser launch. A second spinning disk confocal microscope with a Nikon Plan Apo VC 100x 1.4 oil immersion objective, Nikon LU-N4 laser launch, and Oko Labs Bold Line Cage Incubator with a 96-well plate insert with 0.1% accuracy CO_2 control at 37°C was used to take optogenetic stimulation images and the automated imaging experiments. 488 nm, 561 nm, and 640 nm lasers were used to image mGFP, mCherry, and miRFP670 constructs, respectively, on both microscopes.

Optogenetic stimulation

Specific regions in the nuclei of cells were locally activated by using a Mightex Polygon digital micromirror device (DMD) to pattern blue light (488 nm) activation from a Lumencor SpectraX light engine. U2OS cells expressing FUS_N-miRFP670-TRF1, NLS-GFP-iLID-Fe and FUS_N-mCherry-SspB were imaged using a specific local activation protocol: 1) Pre-activation, imaging the mCherry (541 nm) and miRFP670 (640 nm) channels every 5 s for 10 s; 2) Activation, using a circular region of interest (ROI) (with diameter of 1.2 μm) to locally activate two genomic loci/nuclear bodies to seed, grow, and fuse FUS_N Corelet condensates using the 485 nm DMD every 5 s for 2-10 min; 3) De-activation, back to only imaging the 561 and 640 nm channels every 5 s to allow the FUS_N Corelet condensates to dissolve and pull together attached loci/structures.

Automated imaging protocol

All automated imaging protocols were created by using the JOBS module of the Nikon NIS-Elements software. All protocols included this workflow: 1) Define well selection, 2) Set up the autofocus, 3) Designate the 541 nm and 640 nm lasers as the 'Capture Definition,' and 3) Pre-define points with cells expressing all relevant constructs listed above in the optogenetic stimulation section. Each of the following automated imaging protocols used the DMD to stimulate at pre-defined ROIs at 395 nm wavelength at 30% intensity unless noted otherwise:

Sliding box

In order to mimic a slow scan across a cell from left to right, we defined a rectangular box (1.2 μm wide, 64 μm tall boxes) as the ROI and stimulated two of these boxes at a time with one box remaining from the previous activation sequence to maintain condensates formed from the previous sequence and the second box to form new condensates in the current loop). For each predefined point, the JOBS protocol took a Z-stack before and after the optogenetic activation/de-activation segment. After the first Z-stack, cells were imaged with two ROI boxes for 2-5 min (5 sec/frame) using the Capture Definition ND Stimulation with Sequential Stimulation feature every second. The ND Acquisition sequence was then used to image cells for the de-activation segment (5 sec/frame) for 5 minutes.

Array patterning

The array patterning protocol used the following parameters on the Polygon pad: 0.405 μm diameter of the stimulation ROI with each ROI 2.835 μm apart from its closest neighboring ROI with the array pattern covering an area of 56.7 μm by 56.7 μm of the field of view. The protocol stimulated the ROIs using the 395 nm wavelength at 100% intensity. Cells were imaged for 10 minutes (5 sec/frame).

All telomere stimulation

All telomeres were detected using the 'Bright spot detection' with the NIS-Elements General Analysis 3 program. All bright spots were then converted into ROIs and the same workflow laid out in the 'sliding box' section was applied.

Detect close telomere pairs

Each telomere was detected similarly as the 'All telomere stimulation' protocol. Using General Analysis 3, each bright spot's centroid x, y positions were measured and two bright spots whose centroids were 10 pixels (1.35 μm) or less apart were connected with a thin line. These measurements made and overlaid a binary image of these connecting lines on the telomere channel that were then converted into ROIs for stimulation.

Limitations of preceding automated activation protocols

First, we attempted a global activation pattern across the entire nucleus, which results in Corelet condensates nucleating at each telomere, but infrequent condensate coalescence events due to small overall condensate size (Figure S1B, Global). The smaller an area of the nucleus that is activated, the larger each condensate grows; in our next attempt we activated a smaller rectangular region, then shifted the activation region of interest (ROI) across the nucleus over time to activate the nuclear area sequentially (Figure S1B, Sliding box). This sliding box pattern resulted in larger condensates that do fuse, but is prohibitively time-consuming at 60 minutes per nucleus. Next, we tested an array pattern of activation sites, reasoning that some of the array positions will nucleate between closely positioned telomeres and lead to coalescence events (Figure S1B, Array); while this pattern does sporadically create condensates at productive locations, most are not aligned with telomere loci positions, and thus its efficiency in merging multiple condensates associated with telomeres is low. The best approach for successful repositioning was to identify close telomere pairs at most 1.4 microns apart using a feedback protocol and to only activate those identified pairs, forming condensates at those positions (Figure S1B, Activate each locus).

Physical model

We perform simulations of pulling and merging condensates with the Corelet system via capillary forces, using a phase field model coupled with linear viscoelastic models. The Corelet construct consists of a ‘core’ (A) with 24 binding sites that can bind to the IDR component (B) when light-activated due to iLID-SspB association.[42] The other component of interest is the telomere and the telomere binding protein (FUS$_N$-TRF1), which we treat as a single species that forms a phase that is distinct from the Corelet condensate, and which we intend to move via capillary forces due to its interaction with the condensate. All other species are considered as the buffer (S). We model the mixture using the Flory-Huggins free energy of mixing Δg.[55,87] When there is no light activation, A and B do not associate, and thus do not undergo phase separation. When light-activated, A and B bind (A + B → AB), and the majority exists in the associated form AB which forms the Corelet droplet. Hence for simplicity, we set the interaction parameter between A, B, and other species to zero and only consider the interaction parameter between AB, C, and S,

$$\frac{\Delta g}{k_B T} = \frac{\phi_A}{v_A} ln\ \phi_A + \frac{\phi_B}{v_B} ln\ \phi_B + \frac{\phi_{AB}}{v_{AB}} ln\ \phi_{AB} + \frac{\phi_C}{v_C} ln\ \phi_C + \frac{\phi_S}{v_S} ln\ \phi_S + \chi_{AB,S}\phi_{AB}\phi_S + \chi_{C,S}\phi_C\phi_S + \chi_{AB,C}\phi_{AB}\phi_C \qquad \text{(Equation 1)}$$

where Δg is the free energy of mixing per lattice site based on the Flory-Huggins lattice theory, k_B is the Boltzmann constant, T is the temperature, ϕ_i is the volume fraction of component i, where $i \in \{\text{A, B, AB, C, S}\}$, v_i is the number of lattice sites occupied by species i, and $\chi_{i,j}$ is the Flory interaction parameter between component i and j. The volume fractions satisfy the constraint that $\sum_i \phi i = 1$. For a phase-separating system, in addition to the bulk Δg, the total free energy of mixing also includes the contribution from the concentration gradient, which we assume to have the same coefficient λ^2

$$\Delta G = c_0 k_B T \int \left[\Delta\tilde{g} + \frac{1}{2}\lambda^2 \sum_j \left|\nabla\phi_j\right|^2 \right] dV, \qquad \text{(Equation 2)}$$

where c_0 is the number density of lattice sites, and $\Delta\tilde{g} = \Delta g / k_B T$ is the non-dimensionalized bulk free energy. This free energy is used by Cahn and Hilliard for non-uniform systems and in Cahn-Hilliard equation,[88] which is conventionally used to model phase separation. Due to the energy associated with the concentration gradient, the diffuse interface between phases is on the order of λ.

We define the chemical potential to be the variational derivative

$$\mu_i = {c_0}^{-1} \frac{\delta\Delta G}{\delta\phi_i} \qquad \text{(Equation 3)}$$

Notice that the variational derivative is taken while satisfying the $\sum_i \phi_i = 1$ constraint, in other words, the buffer is treated as a reference component whose volume fraction is a function of those of other components $\phi_S = 1 - \sum_{i \neq s} \phi_i$. We define the activity a_i by

$$\mu_i = \frac{k_B T}{v_i} \ln a_i \qquad \text{(Equation 4)}$$

The equilibrium condition for the association reaction A + B → AB is $a_A a_B = K_d\, a_{AB}$, where K_d is the dissociation constant that changes with the light intensity. The kinetics of association can be described by a rate that follows detailed balance $R = k(a_A a_B - K_d a_{AB})$.[89] Both the kinetic prefactor k and the dissociation constant K_d depend on the light intensity, which we denote with subscripts “on” and “off” to refer to when the light is on ($R = k_{on}(a_A a_B - K_{d,on}\, a_{AB})$) and off ($R = k_{off}\,(a_A a_B - K_{d,off}\, a_{AB})$). Suppose the association is a volume-conserving reaction, that is, $v_{AB} = v_A + v_B$. As modeled previously for light-activated droplet systems,[89] the gradient in the chemical potential causes a diffusive flux and we assume a constant mobility M_i for species i. In summary, the governing equations for all the species are

$$\frac{\partial\phi_A}{\partial t} = \frac{M_A}{k_B T}\nabla^2\mu_A - v_A R \qquad \text{(Equation 5)}$$

$$\frac{\partial\phi_B}{\partial t} = \frac{M_B}{k_B T}\nabla^2\mu_B - v_B R \qquad \text{(Equation 6)}$$

$$\frac{\partial\phi_{AB}}{\partial t} = \frac{M_{AB}}{k_B T}\nabla^2\mu_{AB} + v_{AB} R \qquad \text{(Equation 7)}$$

$$\frac{\partial\phi_C}{\partial t} = \frac{M_C}{k_B T}\nabla^2\mu_C \qquad \text{(Equation 8)}$$

The model above considers C to be a freely moving fluidic species. However, we are also interested in the case where C interacts with certain regions of the chromatin, such as telomeric chromatin. Because TRF1 binds to telomeric DNA, which may experience viscoelastic forces, we model the interaction between C and the telomere using an isotropic interaction kernel $K(|\mathbf{r}-\mathbf{r}_i|)$, which acts as a potential well around the telomere that TRF1 binds to, where $\mathbf{r}$ is any point in space as defined above, and $\mathbf{r}_i$ is the center of the telomere locus i. In other words, extending Equation 2, the total free energy is now

$$\Delta G' = c_0 k_B T \int \left[\Delta\tilde{g} + \frac{1}{2}\lambda^2 \sum_j \left|\nabla \phi_j\right|^2 + \sum_i \phi_c K(|\boldsymbol{r} - \boldsymbol{r_i}|) \right] dV \qquad \text{(Equation 9)}$$

where the summation over i refers to all the telomere loci of interest. Here, we use a Gaussian interaction kernel $K(|\boldsymbol{r} - \boldsymbol{r_i}|) = U_0 \exp - \left(|\boldsymbol{r} - \boldsymbol{r_i}|^2/\lambda^2\right)$, which has the same length scale as the diffuse interface. Note that U_0 is dimensionless.

Due to the interaction between the telomere and the droplets, the droplets also exert a force $\mathbf{F}_i$ on the telomere:

$$\mathbf{F_i} = -\frac{\partial \Delta G'}{\partial \boldsymbol{r_i}} = -c_o k_B T \int \phi_C \frac{\partial K}{\partial \mathbf{r_i}} dV \qquad \text{(Equation 10)}$$

The equation of motion of the center of the telomere locus can be described using various viscoelastic models which we study later:

$$\text{Newtonian}: \eta_i \dot{\mathbf{r}}_{\boldsymbol{i}} = \mathbf{F}_{\boldsymbol{i}} \qquad \text{(Equation 11)}$$

$$\text{Kelvin-Voigt}: \eta_i \dot{\mathbf{r}}_{\boldsymbol{i}} + E_i(\mathbf{r}_i - \mathbf{r}_{i0}) = \mathbf{F}_\text{i} \qquad \text{(Equation 12)}$$

$$\text{Maxwell}: E_i(\mathbf{r}_i - \mathbf{r}_{i0}) = \mathbf{F}_i \text{ and } \eta_i{}' \dot{\mathbf{r}}_{i0} = E_i(\mathbf{r}_i - \mathbf{r}_{i0}) \qquad \text{(Equation 13)}$$

$$\text{Jeffreys}: \eta_i \dot{\mathbf{r}}_{\boldsymbol{i}} + E_i(\mathbf{r}_i - \mathbf{r}_{i0}) = \mathbf{F}_\text{i} \text{ and } \eta_i{}' \dot{\mathbf{r}}_{i0} = E_i(\mathbf{r}_i - \mathbf{r}_{i0}) \qquad \text{(Equation 14)}$$

where the dot refers to the time derivative, E_i is the stiffness constant of the spring element, η_i is the friction coefficient (inverse mobility) of the dashpot, $\eta_i{}'$ is the friction coefficient of the additional dashpot in series with dashpot in the Maxwell and Jeffreys models.

The time scales of these models are important to consider and have significant impact on the dynamics. Therefore, we define them here. Because we are interested in the dissolution and coalescence time of the Corelet condensate, we define time scales based on R_0, defined to be half the distance between the two telomere loci which are located on opposite sides of and in contact with the synthetic condensate, or approximately the radius of it.

The diffusion-limited dissolution/growth time scale of the condensate can be derived based on the Cahn-Hilliard equation (eliminating the reaction term in Equations 5, 6, and 7) to be $\sim \frac{R_0^3 c_0 k_B T}{M_{AB}\gamma}$,[90] where γ is the interfacial tension between the condensate and the buffer phase. In the Cahn-Hilliard formulation, the interfacial tension is defined by the excess free energy per unit area between two phases at equilibrium that form a flat interface. By integrating in the normal direction of the interface from one phase to another,

$$\gamma = c_0 k_B T \int_{-\infty}^{\infty} \left[\Delta\tilde{g} + \frac{1}{2}\lambda^2 \sum_j \left|\nabla \phi_j\right|^2 - \sum_j \mu_{j0}(\phi_j - \phi_{j0}) \right] dx \qquad \text{(Equation 15)}$$

where μ_{j0} is the chemical potential of component j, ϕ_{j0} is the volume fraction of component j in either phase far away from the interface. It can be shown that $\gamma \sim \lambda c_0 k_B T$.[88,91] Therefore, we define a characteristic diffusion time scale $t_d \equiv R_0^3/(M_{AB}\lambda)$. Similarly, the reaction-limited dissolution/growth time scale of the condensate can be derived based on the Allen-Cahn equation (eliminating the diffusion term in Equations 5, 6, and 7) $t_r \equiv R_0^2/(k_{off}\lambda^2)$.[90] Based on the diffusion and reaction time, we define Damköhler number $\text{Da} \equiv t_d / t_r = k_\text{off} R_0 \lambda / M_\text{AB}$.

The equation of motion of the center of the telomere locus using the Newtonian model motivates us to define another viscously dominated coalescence time $t_{v,i}$. Because the length scale of the interaction kernel is λ, depending on the dimensionality ν, the force $|\mathbf{F}_i| \sim c_0 k_B T \lambda^{\nu-1}$. Therefore, based on Equation 11 ($\eta_i R_0/t_{v,i} \sim |\mathbf{F}_i|$), we define $t_{vi} \equiv R_0\eta_i/(c_0 k_B T \lambda^{\nu-1})$.

We may define a dimensionless stiffness constant based on the ratio of the elastic force $\sim R_0 E_i$ and capillary force ($|\mathbf{F}_i|$ above), $\tilde{\mathrm{E}}_i \equiv R_0 E_i/(c_0 k_B T \lambda^{\nu-1})$. Similarly, for the Kelvin-Voigt and Maxwell models, we define the retardation time $\tau_i = \eta_i/E_i$, and the Maxwell relaxation time $\tau_{Mi} = \eta_i{}'/E_i$. We nondimensionalize these time scales by t_d.

We visualize the simulation in images and movies where the red (R), green (G), and blue (B) values are $\text{R} = \text{B} = \phi_\text{C}$, $\text{G} = \phi_\text{A} + \phi_\text{B} + \phi_\text{AB}$, in other words, magenta is used to denote component C, and green is used to denote the Corelet concentration. The kymographs show the simulation results at the symmetry line connecting the two telomere loci over time.

Here, we provide a summary of the simulations and the corresponding dimensionless parameters.

Base case simulation

The purpose of the first simulation is to illustrate the possibility that capillary forces can reposition attached objects. A simulation using the dashpot model reproduces the merging of two telomeres pulled by the condensate, shown in Figure S4C. Denoting the interfacial tension between the AB-rich (C-rich) phase and the buffer-rich phase by $\gamma_{AB,S}$ and $\gamma_{C,S}$, and that between the AB-rich and C-rich phases by $\gamma_{AB,C}$, then bringing AB-rich and C-rich phases into contact, the affinity between the AB-rich and C-rich phases can be quantified by $\gamma_{AB,S} + \gamma_{C,S} - \gamma_{AB,C}$. In the Cahn-Hilliard formulation, the interfacial tensions defined in Equation 15 are related to the interaction parameters χ_{ij}.[91] In Figure S4C, $\chi_{AB,S} = \chi_{C,S} = \chi_{AB,C} = 2$.

Because we are interested in the capillary interaction between the condensate and the chromatin locus, we choose a set of thermodynamic parameters that can give the desired capillary adhesion between components AB and C qualitatively. The precise quantification of the saturation concentration and phase diagram[42,43] is beyond the scope of the modeling here. For the base case simulation where AB is the FUS$_N$ Corelet condensate (FUS$_N$-mCh-SspB + iLID-GFP-Fe, in activated/interacting state), C is FUS$_N$-miRFP670-TRF1, $\chi_{AB,S} = 3$, $\chi_{C,S} = 3$, $\chi_{AB,C} = 2$, $v_A = v_B = v_S = 1$, $v_{AB} = v_C = 2$. Suppose when under light activation the association between A and B is strong and $K_d = K_{d,on} = 0$, $k = k_{on}$, while when not illuminated $K_d = K_{d,off} = 0.2$, $k = k_{off}$. Based on the free energy of mixing (Equation 1) and the volume fraction, the activities of A and B are on the order of 10^{-2} while that of AB is on the order of 1. In order for the initial rate of association $\sim k_{on} a_A a_B$ when light is turned on and the initial rate of dissociation $\sim k_{off} K_{d,off}\, a_{AB}$ when light is off to have the same order of magnitude, we set $k_{on}/k_{off} = 4 \times 10^3$.

We make the assumption that the diffusivity of component C is the same as that of the Corelet condensate component (AB). Based on the measurement of the diffusivities of FUS$_N$-mCh-SspB and iLID-GFP-Fe[S12], we set $M_A = M_B = 10M_{AB} = 10M_C$. For the base case, we set the average composition to be $\phi_A+\phi_B+\phi_{AB} = 0.164$, $\phi_C = 0.041$, and suppose the constituents (A and B) of the condensate have the same volume fractions.

For the time scale, we set $\mathrm{Da} = t_r/t_d = 2000$; $t_{v1}/t_d = t_{v2}/t_d = 0.02$, that is, the two telomere loci have the same inverse mobility and are set to a small value so that it does not have a significant effect. Without yet considering the viscoelastic properties, we use the Newtonian model for the base case. Here in this section, the purpose of the simulation is to illustrate the possibility that telomere droplets can be pulled to merge with capillary forces. The ratios of time scales above remain to be studied and validated in later sections given other experimental evidence.

The simulations are performed in a 2D periodic $L \times L$ domain to capture the dynamics qualitatively. For the base case $L/\lambda = 36$. $R_0/\lambda = 9$. As an example, in Figure 4 $R_0 \approx 0.245$ μm, which corresponds to $\lambda \approx 27$ nm. Initially, the system is fully equilibrated with the presence of two droplets that are rich in component C (which represents the FUS$_N$-TRF1-marked telomeres that are observed in microscopy and henceforth called droplet C) and the light is off. With the imposed average composition, the radii of droplet C are 2.5λ (defined by the region where $\phi_C > 0.5$). Their centers are located at $\mathbf{r}_1(t = 0) = [-d_0/2, 0]$, $\mathbf{r}_2(t = 0) = [d_0/2, 0]$, where $d_0/\lambda = 26$. At $t = 0$, a circular region $\{|r| \le d_0/2\}$ is illuminated. Upon light activation, two Corelet droplets that are rich in AB nucleate in the circular region next to the telomeres. We let the system fully equilibrate until the two droplets merge and form a single condensate in between the two telomere loci. The distance between the two telomere loci becomes $2R_0$, where $R_0/\lambda = 9$, and then turn off the light and let the condensate dissolve. The equations are solved on a grid of [128,128], that is, the grid spacing is 0.3λ.

In the following sections where we study the effect of certain parameters, other parameters remain unchanged unless otherwise stated.

Differential levels of adhesion

Increasing $\chi_{AB,C}$ is expected to increase the energy of interaction between AB-rich phase and C-rich phase and hence the interfacial tension $\gamma_{AB,C}$, resulting in a decrease in the affinity between AB-rich and C-rich phases, modeling the changes in the condensate and telomere loci. We performed two pairs of control simulations where the only difference between them is the value of $\chi_{AB,C}$. We see that when $\chi_{AB,S} = \chi_{C,S} = \chi_{AB,C} = 2$, the adhesion between the telomere and Corelet droplet is strong, the telomeres stay attached to the condensate and eventually merge (Figures S4C and S4E), whereas when $\chi_{AB,S} = \chi_{C,S} = 2$, $\chi_{AB,C} = 3.5$, the telomeres detach and do not merge (Figures S4D and S4F). In Figures S4C and S4D, additional parameters are chosen to match the observed length and time scales in Figures 1A and 2A, while as a control experiment to illustrate the effect of adhesion, Figures S4E and S4F have identical parameters except for $\chi_{AB,C}$.

Specifically, compared to Figure S4C, in Figure S4D we increase $\chi_{AB,C}$ to 3.5 and keep all parameters identical to the 'base case simulation' section except for the sizes of droplets and the average composition to better reflect the relevant experimental length and time scales: the average compositions are $\phi_A + \phi_B + \phi_{AB} = 0.141$, $\phi_C = 0.038$. The distance between the two telomeres initially is $d_0/\lambda = 27.3$. The illumination region is $\{|r| \le d_0/2\}$. When the two Corelet droplets merge into a single droplet, the merged droplet radius is 6.7λ. Again, t_r and t_d are still defined using $R_0 = 9\lambda$ as the characteristic length scale. For reasons we will explain in the 'single telomere interaction with condensate' section, we increase the viscous resistance of the telomere loci to $t_{v1}/t_d = t_{v2}/t_d = 1$, and increase the Damköhler number to $\mathrm{Da} = t_r/t_d = 10^4$ in order to slow down droplet dissolution because, at this level of viscous resistance, it becomes easier for the telomere to detach even for the base Flory interaction parameter of $\chi_{AB,C} = 2$.

To illustrate the effect of $\chi_{AB,C}$, we perform a controlled pair of simulations where the only difference is $\chi_{AB,C}$ shown in Figures S4E and S4F. The average compositions are identical and set to $\phi_A + \phi_B + \phi_{AB} = 0.167$, $\phi_C = 0.038$, and the initial distance to $d_0/\lambda = 26.7$. The illumination region is $\{|r| \le d_0/2\}$.

Single telomere interaction with condensate

Inspired by experiments shown in Figure 2E, we investigated single telomere-condensate interactions (Figures S4G and S4H). When $\chi_{AB,C} = 2$, the singular telomere remains attached to the condensate, but it detaches when $\chi_{AB,C} = 4.7$ (Figure S4H). We studied the effect of viscous resistance and found that the displacement of the telomere toward the condensate decreases with increasing viscous resistance (Figure S4G). The small telomere displacement seen in Figure 2E indicates the resistance experienced by the telomere is high compared to the condensate.

Specifically, the domain size remains the same as the base case. The average volume fraction of C is increased such that the initial radius of the C-rich phase is $R_t = 4.3\lambda$, while the average volume fraction of A and B remains the same as the base case. $\mathrm{Da} = 10^4$ is the same as what is laid out in the Differential levels of adhesion" section. Initially, the single telomere is placed at $[-3.3\lambda, 0]$. The illumination region is $\{|\mathrm{r}| \leq d_0/2\}$ (where $d_0/\lambda = 26$, the same as the base case). All other parameters are the same as the base case.

In Figure S4G, we study the effect of the viscous resistance η_1 by changing t_{v1}/t_d, where the subscript 1 refers to the only telomere locus that is considered here. In the inset, we show the kymographs of the process of Corelet dissolution ($t = 0$ corresponds to the moment when light is turned off) at various values of t_{v1}/t_d. The small telomere displacement seen from experiments in Figure 2E in the main text indicates the resistance to telomere motion is high. This is the reason that in the 'different levels of adhesion between droplets' section we set $t_{v1}/t_d = 1$.

In Figure S4H, setting $t_{v1}/t_d = 1$, we compare single telomere-condensate simulations with $\chi_{AB,C} = 2$ and $\chi_{AB,C} = 4.7$. For both cases, the Corelet condensate nucleates next to the telomere when the light is turned on. During condensate dissolution, when $\chi_{AB,C} = 2$, the condensate stays attached to the telomere, due to the stronger adhesion between the two, however, when $\chi_{AB,C} = 4.7$, the weak adhesion causes the condensate and telomere to detach from one another.

Models of chromatin viscoelasticity

Next, we consider models of viscoelasticity including Kelvin-Voigt (Equation 12) and Jeffreys model (Equation 14). Consistent with the 'single telomere interaction with condensate' section, we set $\mathrm{Da} = 10^4$, and all other parameters are identical to the base case. For better agreement with experiments shown in Figure 4A, namely the distance moved before telomeres detach, we choose normalized retardation time $\tau_1/t_d = \tau_2/t_d = 2$, and dimensionless resistance $\tilde{\mathrm{E}}_1 = \tilde{\mathrm{E}}_2 = 0.4$, where the subscripts 1 and 2 refer to the two telomere loci. For the comparison between Kelvin-Voigt and Jeffreys models, we vary the normalized Maxwell relaxation time $\tau_M/\, t_d$ (Figure S4I), (where $\tau_M = \tau_{M,1} = \tau_{M,2}$ is the Maxwell relaxation time for both telomere loci). The Kelvin-Voigt model is a special case of Jeffreys model with $\tau_{M,i} = \infty$. We see that the amount of recoil lessens with decreasing the Maxwell relaxation time. Kymographs predicted by the Kelvin-Voigt model ($t_d/\tau_M = 0$), which predicts that the telomere recoils back to its original position, and the Jeffreys model ($t_d/\tau_M = 0.8$), which predicts a partial recoil, are shown in Figures 4B and 4C.

We do not consider the Maxwell model here because if the impedance on the telomere is described completely by the Maxwell model, then the telomere will exhibit an instantaneous recoil when the condensate detaches. Notice that in our model, the dynamics of the center of telomeric chromatin ($\mathbf{r}_i$) and that of TRF1 (component C) are modeled separately, the overall impedance is contributed by both. In our physical model, using a Maxwell model (or a spring model) for the telomeric chromatin will not cause instantaneous recoil, but the recoil dynamics will be faster than a Jeffreys model that has the same spring and dashpot connected in series but with an additional dashpot in parallel. Thus, the retardation time τ/t_d controls the speed of the recoil dynamics and using the Maxwell model is equivalent to setting $\tau_1/t_d = \tau_2/t_d = 0$.

Asymmetric viscoelastic resistance

In Figures S5D–S5K, we analyze the asymmetry of viscoelastic properties. We make the assumption that a telomere near the nuclear periphery experiences a proportionately higher spring stiffness and viscous friction, that is, when using the Kelvin-Voigt model, we assume $\rho_2/\rho_1 \equiv E_2/E_1 = \eta_2/\eta_1$, hence the definition of ρ_2/ρ_1 in the main text. Since $t_i = \eta_i/E_i$, this assumption is equivalent to $t_1 = t_2$.

First, we use the Kelvin-Voigt model, set the retardation time on both sides to be equal $\tau_1/t_d = \tau_2/t_d = 2$ and fix the normalized stiffness on one side $\tilde{\mathrm{E}}_1 = 0.05$ while varying $\tilde{E}_2$. The trajectory $x(t)$ of the two telomeres in this Kelvin-Voigt model is shown in Figure S5D. We define Δx_i to be the distance that the telomere travels from $t = 0$ to the moment when the two telomere merge, defined to be the time point with the highest $\left|d^2x/dt^2\right|$, indicated by the filled circles (Figure S5D). The ratio $\Delta x_1/\Delta x_2$ increases linearly with increasing $\tilde{\mathrm{E}}_2/\tilde{\mathrm{E}}_1 = \rho_2/\rho_1$ (Figure S5E). Considering the resistance of the condensate in between the two telomeres, we use a simple model to predict the asymmetry in the displacement given the asymmetry in the viscoelastic properties:

$$\frac{\Delta x_1}{\Delta x_2} \approx \frac{\tilde{E}_2 + \tilde{R}}{\tilde{E}_1 + \tilde{R}} \qquad \text{(Equation 16)}$$

where R is the effective resistance of the condensate relative to that of the telomeric chromatin. Fitting these data to Equation 16, we obtain R = 0.029.

Next, we fix the ratio of the stiffness constants $\tilde{\mathrm{E}}_2/\tilde{\mathrm{E}}_1 = 5$ and vary $\tilde{E}_1$. Figure S5F shows the trajectories and Figure S5G shows that the ratio $\Delta x_1/\Delta x_2$ gradually increases and reaches a plateau with increasing $\tilde{E}_1$. Therefore, when the resistance from the chromatin dominates over that of the condensate, which is likely the case given the negligible displacement of the telomere when a single telomere is attached to the Corelet droplet as it dissolves, the ratio of displacement becomes closer to the inverse ratio of the stiffness ($\tilde{E}_2/\tilde{E}_1$). Fitting the data to Equation 16, we obtain R = 0.030.

In Figures S5H–S5K, we repeat the analysis above using the Jeffreys model. Again, we assume that all dashpot and spring elements have proportionately higher values near the nuclear periphery, that is, $\rho_2/\rho_1 \equiv E_2/E_1 = \eta_2\eta_1 = \eta_2^{`}/\eta_1^{`}$. In other words, both telomeres have the same retardation time and Maxwell relaxation time. We set $\tau_1/t_d = \tau_2/t_d = 2$ and $\tau_{M,1}/t_d = \tau_{M,2}/t_d = 2$. Again, we find that Equation 16 is a good approximation for the ratio of displacement and the fitted value of R is 0.042 and 0.041 in Figures S5I and S5K, respectively.

The consistency in the fitted $\tilde{R}$ indicates that Equation 16 provides a useful estimate of the asymmetry. More importantly, Equation 16 provides an upper bound to the ratio of the displacement equation

$$\frac{\Delta x_1}{\Delta x_2} < \approx \frac{\tilde{E}_2}{\tilde{E}_1} = \frac{\rho_2}{\rho_1} \qquad \text{(Equation 17)}$$

In other words, given the ratio of displacement observed in experiments, Equation 17 provides a lower bound for the ratio of local resistance.

Rouse model

In this section, we consider another model for describing the viscoelasticity of the genomic locus- the Rouse model, which describes the motion of an ideal polymer chain without hydrodynamic interactions. The equation that governs the position of chain x(s), where s is the arc length, is from Keizer et al.[30]

$$\eta \frac{\partial \mathbf{x}}{\partial t} = \kappa \frac{\partial^2 \mathbf{x}}{\partial s^2} + \mathbf{f}(t,s), \qquad \text{(Equation 18)}$$

where η is the friction coefficient, *k* is a coefficient for the stiffness of the chain, **f**(*t,s*) is the force on the chain.

The condensate only interacts with the locus while all other parts of chain are “phantom” that do not chemically interact with other components in this system, hence the capillary force only acts on the locus, which is approximated as a point located at s = 0, that is, **f**(*t,s*) = **F**(t)δ(s), where **F** is the capillary force defined in Equation 10. Consistent with previous simulations, we omitted the thermal noise for simplicity, focusing only on the capillary force. Suppose the chain is infinitely long and initially straight, and using subscript i=1,2 to denote the two loci, then the analytical solution to Equation 18 at the position of the locus r_i(t) = x(t,s = 0) is

$$\mathbf{r}_i(t) = \mathbf{r}_i(0) + \int_0^t \frac{\mathbf{F}_i(t')}{\sqrt{4\pi\eta_i\kappa_i(t-t')}} dt' \qquad \text{(Equation 19)}$$

This dynamic applies to both telomere loci which are assumed to be located on two independent polymer chains. From Equation 19, we find that for infinitely long polymer chains, only one parameter is needed to describe its dynamics and the time scale of relaxation for the Rouse model $t_{rs,i}$ satisfies $R_0 \sim |F_i| \, (t_{rs,i}/(4\pi\eta_i\kappa_i))^{1/2}$, hence we define

$$t_{rs,i} \equiv 4\pi\eta_i\kappa_i \left(\frac{R_0}{c_0 k_B T \lambda^{\nu-1}}\right)^2. \qquad \text{(Equation 20)}$$

Similar to previous sections, we start from the state where the Corelet droplet has merged and study the effect of t_{rs}/t_d on the evolution of the distance between the telomere loci, as shown in Figure S4K. As the resistance of the polymer chain increases (t_{rs}/t_d increases), the displacement of the locus decreases. For large resistances ($t_{rs}/t_d \geq 0.01$), the telomeres detach from the condensate and recoil at about t/t_d =1.4. For small resistances ($t_{rs}/t_d \geq 0.1$), the telomeres merge (Figure S4K). When the telomeres detach and the capillary force vanishes, the recoil dynamics at long times follows $|r(t) - r(0)| \sim t^{-1/2}$ (Figure S4L). In Figure S4M, we show the evolution of capillary force F on the telomere loci in the direction toward each other over time. During condensate dissolution, the pull force increases, and note that for small resistance, the capillary force remains after the condensate has dissolved since adhesion force between the loci is necessary to keep them in place while the polymer chains relax (Figure S4M). Over the range of Rouse polymer relaxation time t_{rs}, the model predicts a spread of recoil dynamics similar to the Jeffreys model, so a Rouse polymer is not inconsistent with the observed range of viscous and elastic recoil recoveries in our experimental data (Figures 4G and 4H).

Repositioning non-chromatin nuclear bodies

A simulation of the Cajal body in Figure S4J uses Equation 2 without the interaction kernel. Parameters are chosen to match the observed length and time scales in Figure S2F. We also perform an additional control simulation comparing the telomere (using Equation 9) and the Cajal body Equation 2 with the only difference being whether the interaction kernel is included. The Coilin construct forms a ring at the interface between the condensate and the buffer (Figure S4J inset), similar to experimental results (Figure S2G).

Specifically, we perform simulations with all the parameters identical to the ‘base case simulation’ section except for the sizes of the condensates and domain and the average composition to better reflect the experimental observation in Figure S2F. The average compositions are $\phi_A + \phi_B + \phi_{AB} = 0.104$, $\phi_C = 0.03$ The domain size is changed to $L/\lambda = 50$. Initially, the radii of the two Cajal bodies are 2.3λ. Their centers are located in the same way as the ‘base case simulation’ section, while the distance is $d_0/\lambda = 33$. The illumination region is again $\{|r| \leq d_0/2\}$. When the two condensates merge into a single droplet, the radius of the merged droplet is 8λ. Note that while the single condensate size is different from R_0 in the ‘base case simulation’ section, t_r and t_d are still defined using $R_0 = 9\lambda$ as the characteristic length scale.

In Figure S4J, we compare the telomere (with interaction kernel) and Cajal bodies (without interaction kernel) using the same exact parameters, average composition, and length scales as defined above.

QUANTIFICATION AND STATISTICAL ANALYSIS

Kymograph production

Time series images of chromatin locus movement were registered to correct for whole cell movement in FIJI (ImageJ 1.52p)[85] using HyperStackReg,[92] Rigid Body translation. A line was drawn across the activation region and kymographs were created using the MultiKymograph plugin.

Loci tracking during repositioning

Registered time series images of chromatin locus repositioning were cropped to a region containing the relevant telomeres, then loaded into the TrackMate plug-in Tinevez et al.[93] in FIJI. Telomeres were identified in the miRFP670 channel with the LoG detector, with an estimated blob diameter of 0.7 microns and no initial thresholding. Spots were filtered by quality to eliminate background. Tracks were generated using Simple LAP tracker with max linking distance 1 micron, gap-closing max distance 1 micron and gap-closing max frame gap 0 frames. Tracks of the relevant telomeres were identified and the XY distance (d) between them calculated for each time point $d = \sqrt{(Y_2 - Y_1)^2 + (X_2 - X_1)^2}$.

Detachment probability

Constructs with $\mathrm{FUS_N}$ point mutants ($\mathrm{FUS_N}^{3YS}$, $\mathrm{FUS_N}^{5YS}$, $\mathrm{FUS_N}^{9YS}$, $\mathrm{FUS_N}^{15YS}$, $\mathrm{FUS_N}^{27YS}$) fused to miRFP670-TRF1 were created, expressed in living U2OS cells along with Corelet components, and imaged using the Optogenetic Stimulation protocol as described above. ROIs were aimed at singular telomere loci to observe how a single locus-condensate pair would behave during condensate dissolution during the de-activation sequence. Chromatin-condensate pairs were classified as ‘attached’ if the condensate dissolved towards the locus or ‘detached’ if the condensate dissolved concentrically, away from the telomere.

Estimating number of IDR-IDR interactions at the chromatin-condensate interface

Previously, we have measured the diameter of telomeres in U2OS cells by super-resolution STED microscopy to be on the order of 100-150 nm (data not shown), in agreement with published estimates of telomere sizes in different cell lines.[94–99] The surface area of an average telomere would then be $4\pi(0.075\mu m)^2 = 0.071\mu m^2$. We estimate from our images that usually less than half of the surface of the telomere is in contact with the Corelet condensate, so the interfacial area between the chromatin and condensate is up to $0.035\ \mu m^2$. Each $\mathrm{FUS_N}$-SspB-decorated ferritin “core” particle has a radius of 20 nm,[42] so a surface area of $0.005\ \mu m^2$. Assuming packed spherical core particles coating the condensate-telomere interface, we estimate that approximately $(0.035/0.0025) = 14$ cores interact with the available surface of the telomere. Every core has binding sites up to 24 $\mathrm{FUS_N}$ IDRs distributed on its surface, up to half of which (12) are in an orientation to interact with the locus-tethered IDRs at any time. These experiments represent a bulk of approximately $14 \times 12 = 168$ condensate IDRs interacting with a similar number of chromatin-tethered IDRs providing the interfacial force between a chromatin locus and condensate.

Detachment probability as a function of strain and velocity

Probability of detachment of single $\mathrm{FUS_N}^{15YS}$-miRFP670-TRF1-marked locus from its attached condensate was separated into bins by strain (0 - 1) and by velocity (0 - 1.0 microns/min). Images were processed in FIJI, using Trackmate to identify the XY position of the locus of interest using the miRFP670 channel and XY position of the condensate centroid using the $\mathrm{FUS_N}^{WT}$-mCherry-SspB channel. Strain was defined as $(d_0\text{-}d_d)/d_0$ where d_0 is the initial distance between the chromatin locus centroid and condensate centroid during the first frame of deactivation, when force application begins, and d_d is their distance at the moment of measurement. Examples which stay attached experienced all possible strains between 0 and 1. Detachment velocity was defined as the linear slope of locus displacement over time for the 10 - 30 seconds before detachment; loci that did not detach were counted as ‘attached’ in the bin within their highest recorded velocity.

Symmetric/asymmetric locus movement characterization

All images were analyzed using FIJI for the image pre-processing steps and Python 3.7.10 for image processing and analysis. During pre-processing, each nucleus was corrected for whole cell movement using HyperStackReg, and set to a contrast level sufficient for segmentation in Python. In Python, the last frame of the activation sequence from the mCherry and miRFP670 channels were used to segment nuclei and telomeres respectively, and repositioned telomeres from the last frame of the de-activation sequence were segmented, then binary nuclear masks were processed with the Canny Edge Detection method to identify the nuclear and nucleolar peripheries from the $\mathrm{FUS_N}^{IDR}$-mCherry-SspB channel. The nucleoli are detectable in this channel as dark spots within the nucleus due to exclusion of the construct from nucleolar regions. The distance from all nuclear and nucleolar edges to telomere centroids in both frames were calculated, and the edge bearing the shortest distance from each telomere was called out and characterized as the point of ‘nearest periphery.’ This information was then used to find the actual distance between the closest edge and telomere of interest $d = \sqrt{(Y_2 - Y_1)^2 + (X_2 - X_1)^2}$. Distances were plotted as a fraction of the total distance between the two telomeres, classified into three distance bins. A telomere pair was classified as 'peripheral' if both telomeres were < 0.5 μm from the periphery of the nuclear/nucleolar periphery, 'internal' if both were > 0.5 μm from the nearest periphery, or 'mixed.'

Heterogeneity in chromatin viscoelasticity

Numerical asymmetric distances moved by each locus were directly converted into a ratio of viscoelastic resistances associated with each locus (ρ_2/ρ_1) using the calibration chart provided by a series of simulations (Figure 5C). These were plotted again in categories 'peripheral', 'internal' and 'mixed' as above.

Hoechst intensity analysis

All images were pre-processed and analyzed as described above in the 'symmetric/asymmetric locus movement characterization' section. Binary nuclear masks were processed in FIJI to obtain the average Hoechst intensity values for the whole nucleus with Python 3.7.10. The first frame of the activation sequence from the miRFP670 channel was used to segment telomeres in their original nuclear positions. Telomere centroids and an area spanning 0.33 microns (2 pixels) radius around each centroid were found to measure local DNA density surrounding each telomere, normalized to that particular nucleus' average. Hoechst intensities of all 2 pixel radius areas were plotted to show the distribution of intensity differences in each individual nucleus with the values corresponding to where the two telomeres experiencing force application are in color. The ratio between Hoechst intensities of the area surrounding each of the two pulled telomeres, always with the higher intensity as numerator, was calculated to be H_2/H_1 measurement plotted against the ratio of the distance traveled by each telomere d_1/d_2 ('Asymmetric Travel'), or against viscoelastic ratio ρ_1/ρ_2.

Mean squared displacement analyses

U2OS cells were transduced with lentivirus to express miRFP670-TRF2, to fluorescently mark telomeres, and imaged 2–3 days post transduction. Telomere tracking time series images for Figures S6A and S6B were obtained by imaging the 670 nm channel every 3 seconds for 30 minutes. In Figures S6D–S6F, images of $\text{FUS}_\text{N}^\text{IDR}$-miRFP-TRF1 labeled telomeres were obtained from non-pulled telomeres in force application time series images, taken in 670 nm channel every 5 seconds for 10-20 minutes. MSD data were analyzed as previously described.[24] Briefly, tracking time series images were cropped to isolate individual nuclei, and processed in FIJI using Trackmate with blob diameter 0.7 μm and intensity threshold 85. LAP tracker was used to build trajectories with maximum frame-linking and gap-closing set to 0.5 μm. For Figures S6D–S6F, the pulled telomeres, identified by eye as the ones interacting with the condensate surface, were manually excluded from MSD analysis. Tracks were exported from Trackmate for further analysis.

Pairwise mean squared displacement (MSD) is defined as a function of time-step τ according to the following equation, where *d(t)* is the distance between the two puncta at time *t*:

$$MSD(\tau) = \langle (d(t+\tau) - d(t))^2 \rangle_t$$

Using a pairwise MSD in lieu of the more traditional single-particle version allows control for translation and rotation of the cell during video acquisition without relying on image registration. MATLAB was used to compute, plot, and fit MSD (τ) curves in Figures S4 and S6. Trajectories shorter than a minimal duration cutoff (1200 seconds for Figure S4 and 500 seconds for Figure S6) were automatically discarded from the analysis; pairs of loci that coexisted for longer than the minimum cutoff were then identified, and MSD (τ) curves were computed for each pair, with maximum τ set at 80 frames. For peripheral vs internal comparison in Figure S6, pairwise MSDs were binned into 'peripheral' and 'internal' categories based on their component telomere's nuclear positioning, determined algorithmically as within 0.45 microns of the nuclear periphery and confirmed visually.

Passive microrheology to determine viscoelastic moduli

We used telomere mean squared displacement data to estimate the order of magnitude of the nuclear interior viscoelastic modulus, G*, according to Equations 10, 11, and 12 in Mason et al.[100]

$$G'(\omega) = |G*(\omega)| cos(\pi\alpha(\omega)/2),$$

$$G''(\omega) = |G*(\omega)| sin(\pi\alpha(\omega)/2),$$

where

$$|G*(\omega)| \approx \frac{k_B T}{\pi a \langle r^2(1/\omega)\rangle \Gamma[1+\alpha(\omega)]}$$

Other studies have used similar approximations on MSD tracking data of peroxisomes from live ATP-depleted cells to estimate the elastic shear modulus G', viscous shear modulus G'', and viscoelastic modulus G* of the cytoplasm at angular frequencies between

0.126 and 628 rad/s.[101] We estimated the telomere's radius to be on the order of 0.1 micron that is consistent with previous studies,[94–99] and frame rate was 3 seconds. Using a public MATLAB code (https://doi.org/10.5281/zenodo.12628456), we calculated from average telomere MSDs of 18 nuclei the apparent elastic and viscous moduli. We call these apparent moduli because the approach assumes thermodynamic equilibrium, so there may be some contribution from out-of-equilibrium (e.g. ATP-dependent) effects. We find the apparent elastic and viscous moduli of chromatin measured via telomere probes are of equivalent magnitudes, with the elastic modulus slightly dominating for lower frequencies. Additionally, we calculate that G* is on the order of 1 Pa (Figure S4C) across angular frequencies between 0.355 and 12.58 rad/s.

Initial order of magnitude force estimation from telomere trajectories

To approximate the magnitude of force applied on a chromatin point locus by a shrinking condensate, we used an estimation method that is based on the generalized Langevin equation under the assumption that thermal fluctuations dominate the noise. From Eq. 1 in Mason and Weitz,[102] ignoring inertia and with the presence of the pulling force *F*(*t*), we have

$$\int_0^t \zeta(t-\tau)v(\tau)d\tau = F(t) - f_R(t) \qquad \text{(Equation 21)}$$

where *t* is time, $\zeta(t)$ is the generalized time-dependent memory function, $v(t)$ is the particle velocity, $f_R(t)$ is the random force that satisfies $\langle f_R(t)\rangle = 0$ and $\langle f_R(0)f_R(t)\rangle = k_BT\zeta(t)$, where k_B is the Boltzmann's constant and *T* is the temperature. Taking the ensemble average of Equation 21, we have

$$\int_0^t \zeta(t-\tau)\langle v(\tau)\rangle d\tau = F(t) \qquad \text{(Equation 22)}$$

During the pull, the experimental telomere displacement curve in Figure 1 shows that the distance between telomere loci approximately decreases linearly in time with a constant velocity $v_0 \sim 1$ μm/min. As an approximation for the ensemble average of the velocity during the pull, $\langle v(t)\rangle \approx v_0$. Hence, during the pull the force is

$$F(t) \approx v_0 \int_0^t \zeta(t)dt \qquad \text{(Equation 23)}$$

Denoting the Laplace transform with a tilde, the Laplace transform of *F*(*t*) is

$$\tilde{F}(s) = \frac{v_0}{s}\tilde{\zeta}(s) = \frac{6k_BTv_0}{s^3\langle\Delta\tilde{r}^2(s)\rangle} = \frac{6\pi a v_0\tilde{G}(s)}{s^2} \qquad \text{(Equation 24)}$$

where *s* is the frequency in the Laplace domain, $\langle\Delta\tilde{r}(t)\rangle$ is the mean squared displacement (MSD) of a tracer particle, and $\langle\Delta\tilde{r}^2(s)\rangle$ is the corresponding Laplace transform, $a \sim 0.1$ μm is the radius of the telomere, consistent with previous measurements as noted above, $\tilde{G}(s)$ is the Laplace transform of the shear modulus. The last two equalities are from Eqs. 3-4 in Mason and Weitz.[102]

As an order of magnitude estimation, from the MSD measured in Figures S5A and S5B, at the frequency of 1 min^{-1}, which is the frequency scale that corresponds to the time window during which the pull force is applied onto the telomere, we have $\tilde{G} \sim 1$ Pa calculated from G* as shown in Figure S5C (see 'passive microrheology to determine viscoelastic moduli' section), hence $F \sim 1$ pN, which is on the same order of magnitude as the forces calculated using the Rousepull method from Keizer et al.[30] (see 'generating pull force estimation plots' section).

Generating pull-force estimation plots

In order to estimate the pull force applied on chromatin loci during the dissolution of the condensate, we referred to "Section II. Force Inference" in Keizer et al.[30] Supplementary Text and utilized corresponding code for force inference (https://github.com/OpenTrajectoryAnalysis/rousepull) provided by Keizer et al.[30] authors. With this "Rousepull" method, we use the Rouse polymer model to infer forces in chromatin loci pulling experiments, calibrating it on our MSD tracking of telomeres in the absence of the condensate (i.e. in the absence of applied force), using prefactor $\Gamma = 0.0021$ $\mu\text{m}^2/\sqrt{\text{s}}$ as a first approximation that was extracted from our telomere tracking MSD data $\langle x^2(t)\rangle = \Gamma\sqrt{t}$ (chromatin loci undergo Rouse diffusion essentially in the absence of the pull force). In Figure 6, we measure the prefactor Γ for each condition (Untreated, TSA-treated, methylstat-treated) through pairwise MSD of all non-pulled telomere loci in pulling time series. Using HyperStackReg[92] in FIJI, we first corrected for whole cell movement, then track the positions of the relevant telomeres in Trackmate (blob size 0.4 microns, initial thresholding 40) and run the Rousepull analysis on the relative motion (i.e. distance between two loci) over time (in seconds) for each pair of loci to obtain estimated force profiles (Figures 4D–4F, 4I, and 6G).

Statistical analysis

Statistics were performed using GraphPad PRISM version 9.1.0 software (GraphPad). Statistical significance of detachment probabilities in Figures 2 and S2 were calculated using a Chi-squared test for trend; p value and size of n are noted in figure legends and captions accordingly. Statistical significance of asymmetric locus movement as a function of locus position was calculated using one-way ANOVA with multiple comparisons, number of replicates, and size of n are noted in the figure legends and captions accordingly.

Supplemental figures

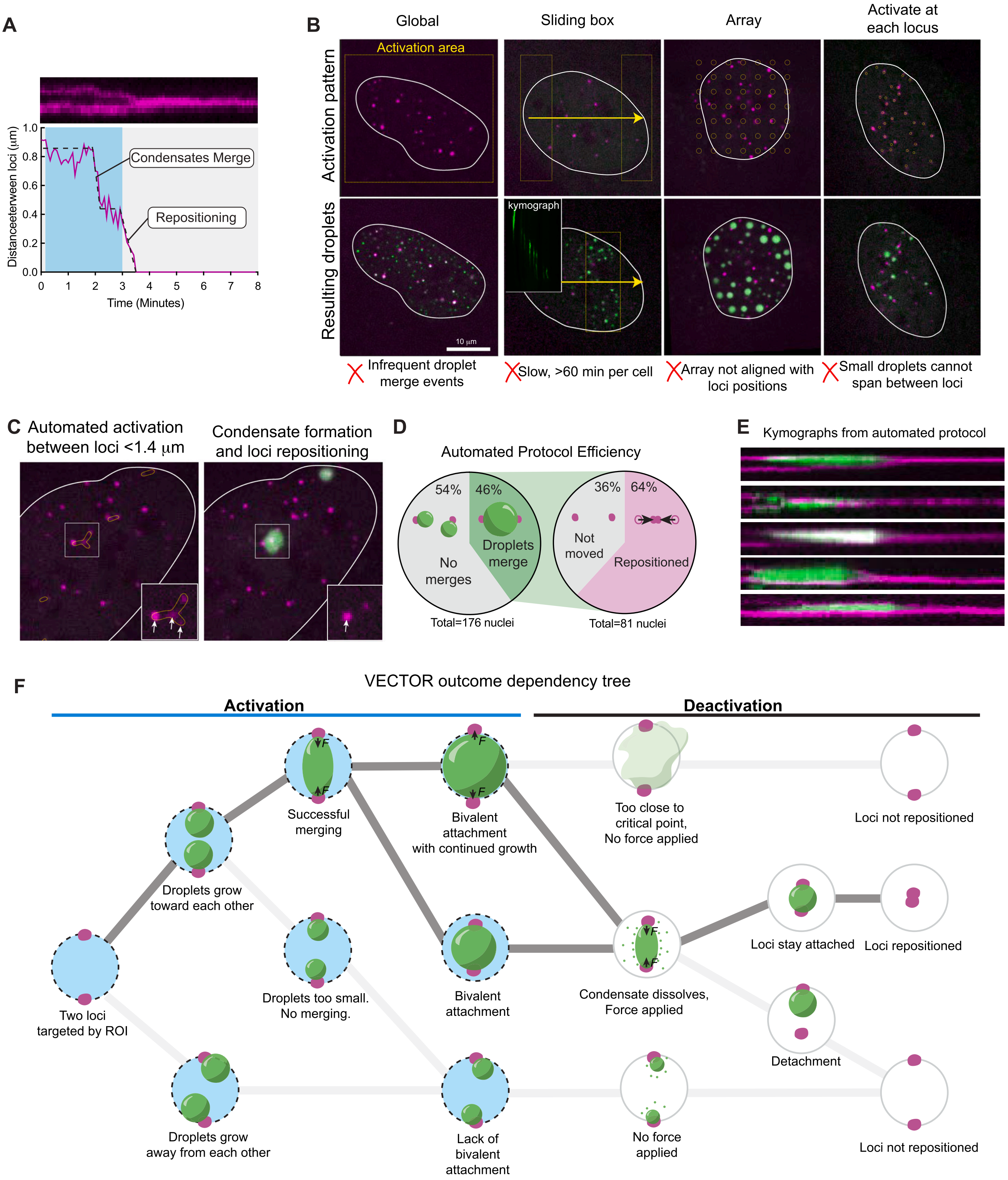

(legend on next page)

Figure S1. A programmable system for repositioning genomic loci, related to Figure 1

Similar to Figure 1: representative images.

(A) Kymograph and a graph showing locus distance over time for a second locus repositioning (yellow box from Figure 1B) in the same cell, demonstrating that multiple pairs of loci can be manipulated at once using VECTOR.

(B) Representative images from iterations of development of an automated imaging protocol with automatically generated activation regions indicated in yellow (top) and resulting condensate pattern (bottom) for light patterns: global, sliding box, array patterning, and activation at each locus.

(C) Representative image of automatically generated activation regions between loci $< 1.4\ \mu m$ apart using a custom JOBS protocol (see STAR Methods).

(D) Quantification of automated light-patterning protocol efficiency. Of 176 nuclei attempted, 81 nuclei, or 46%, produced productive condensate merger events, and of those, 52 nuclei, or 64%, resulted in successful locus repositioning.

(E) Representative kymographs of telomere repositioning initiated by the automated imaging protocol.

(F) Schematic of potential outcomes observed when attempting to reposition two loci using VECTOR, with pathways to productive repositioning highlighted in bold. From left to right, two loci are targeted by an ROI, which grow droplets either toward each other or away from each other. Growth away from each other leads to a lack of bivalent attachment, no force is applied, and loci are not repositioned. If droplets grow toward each other and are large enough to successfully merge into a bivalent attachment, when the light is deactivated, the condensate dissolved, force is applied, and attached loci are repositioned.

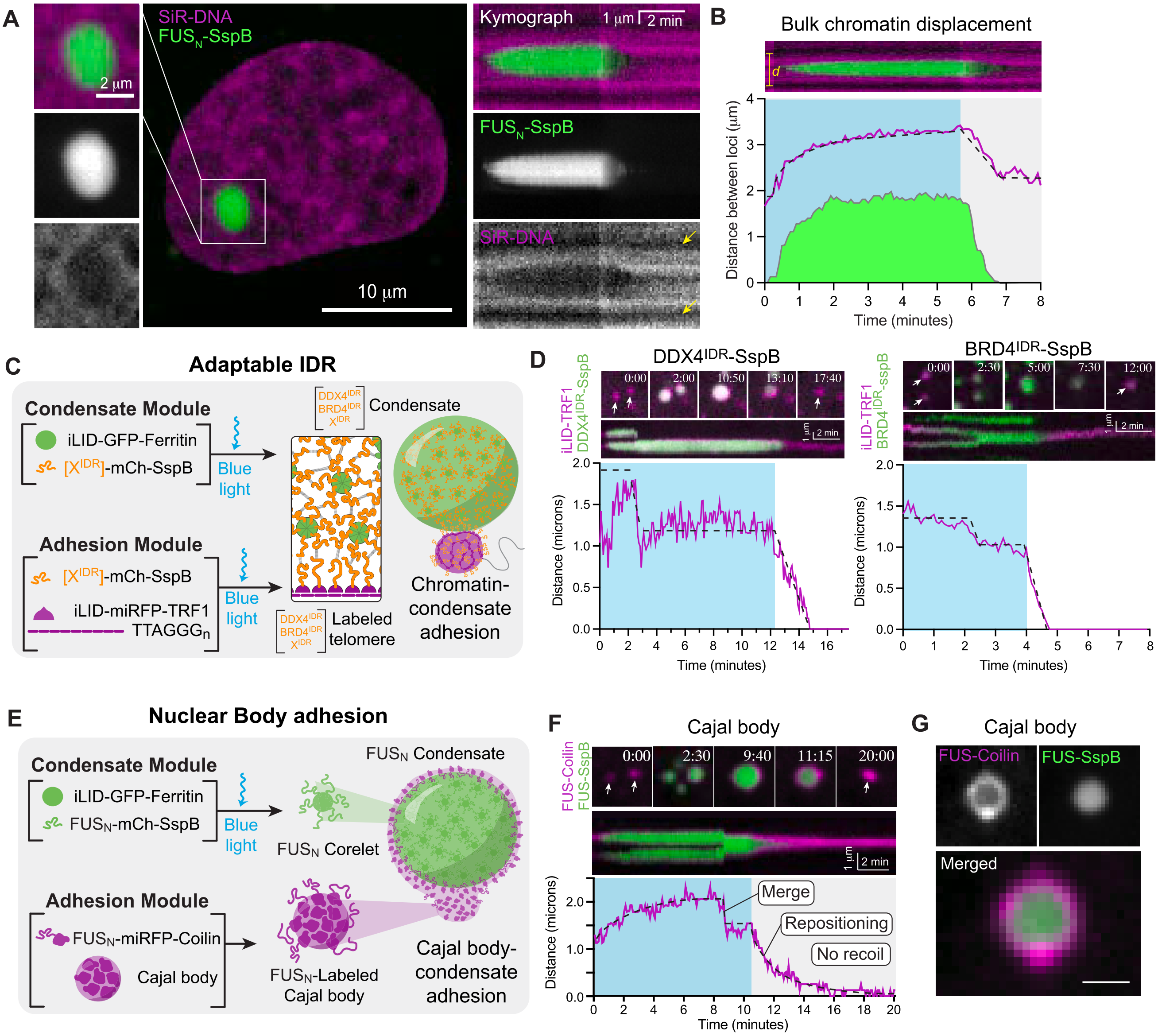

Figure S2. Interchangeable condensate and adhesion modules of VECTOR, related to Figure 2

(A) Marking all chromatin with SiR-DNA reveals that chromatin (magenta) is excluded from the bulk of IDR-based condensates (FUS$_N$-SspB, green), and kymograph shows that chromatin can relax to fill the void as the condensate shrinks.

(B) Plot of distance between two chromatin-poor nuclear features (*d*, yellow distance) shows they are moved apart slightly as a condensate grows between them and relax back to their original positions upon condensate dissolution (magenta). In green is the diameter of the condensate between the tracked features.

(C) Schematic of VECTOR system with adaptable IDR capability; iLID-miRFP670-TRF1 (magenta) recruits *Any IDR*-mCherry-SspB (green) upon light activation, creating adhesion between the repetitive locus and IDR-based condensate.

(D) Example stills and kymographs of successful locus repositioning using iLID-TRF1 with DDX4^{IDR}-mCherry-SspB (left) and BRD4^{IDR}-mCh-SspB (right).

(E) Schematic of VECTOR system that repositions non-chromatin nuclear bodies: Cajal bodies. FUS$_N$-miRFP670-Coilin (magenta) marks Cajal bodies and creates adhesion between them and a FUS$_N$ Corelet condensate (green).

(F) Two FUS$_N$-miRFP670-Coilin bodies (magenta) are repositioned. Merged kymograph shows fusion of the two Cajal bodies. After repositioning, Cajal bodies remain fused until the end of the observation period (20:00, no recoil).

(G) Still images of individual channels of FUS$_N$-miRFP670-Coilin (magenta) and FUS$_N$ condensate (green) exhibiting their core-shell architecture.

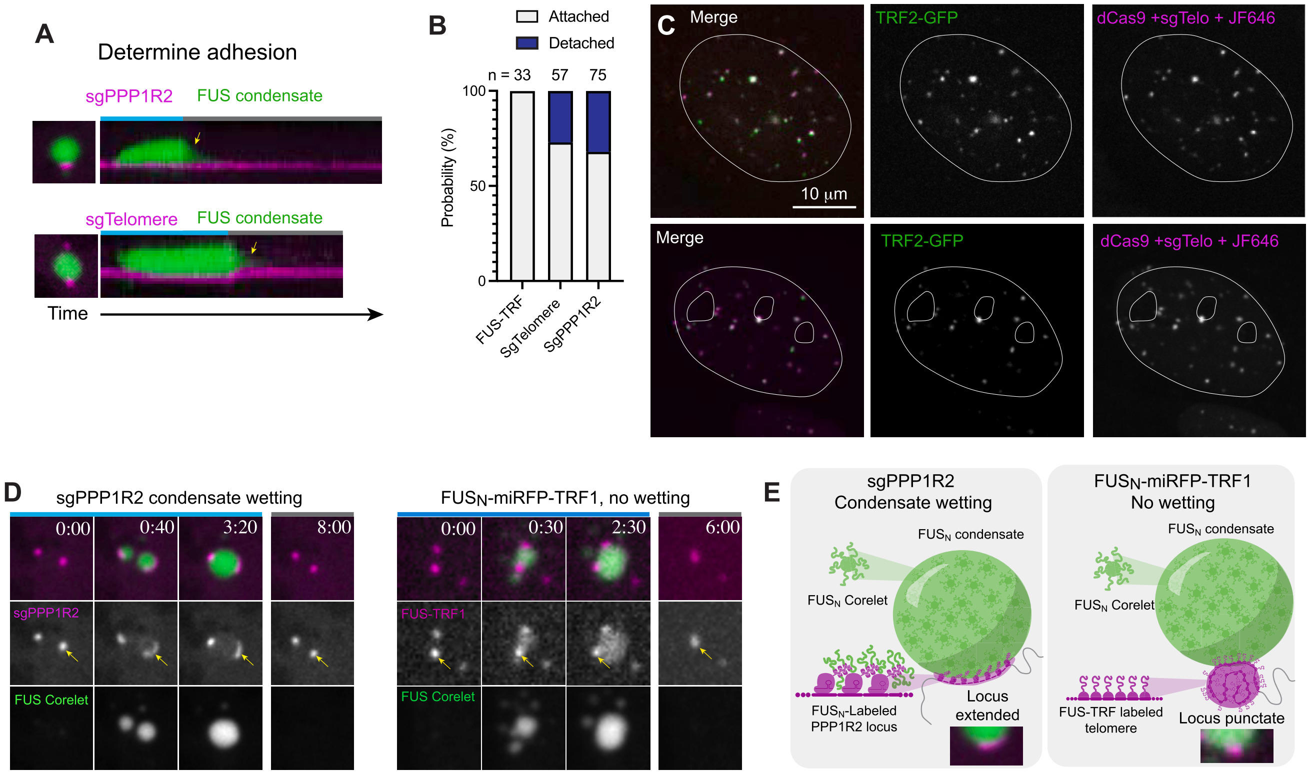

Figure S3. Validation of dCas9-based adhesion module, related to Figure 3

(A) Example kymographs determining locus-condensate adhesion of dCas9-based adhesion module targeted to PPP1R2 locus (top) or telomeres (bottom).

(B) Quantification of detachment probability of dCas9-based adhesion module at telomeric and PPP1R2 loci compared with FUS_N-TRF1-based adhesion module. *N* reported above each condition are the counts of individual droplet-locus interactions.

(C) Representative images of two live example nuclei with telomeres marked by TRF2-GFP (green) and dCas9-based adhesion module targeted to telomeres via sgTelo and visualized with JF646 Halo ligand (magenta).

(D) Stills from a sgPPP1R2 locus movement experiment (left) and a FUS_N-TRF1 telomere locus movement experiment (right) show PPP1R2 locus extension along the surface of the FUS_N condensate (3:20), while FUS_N-TRF1-labeled telomeres remain punctate during surface adhesion (2:30).

(E) Schematics describing locus extension during surface adhesion.

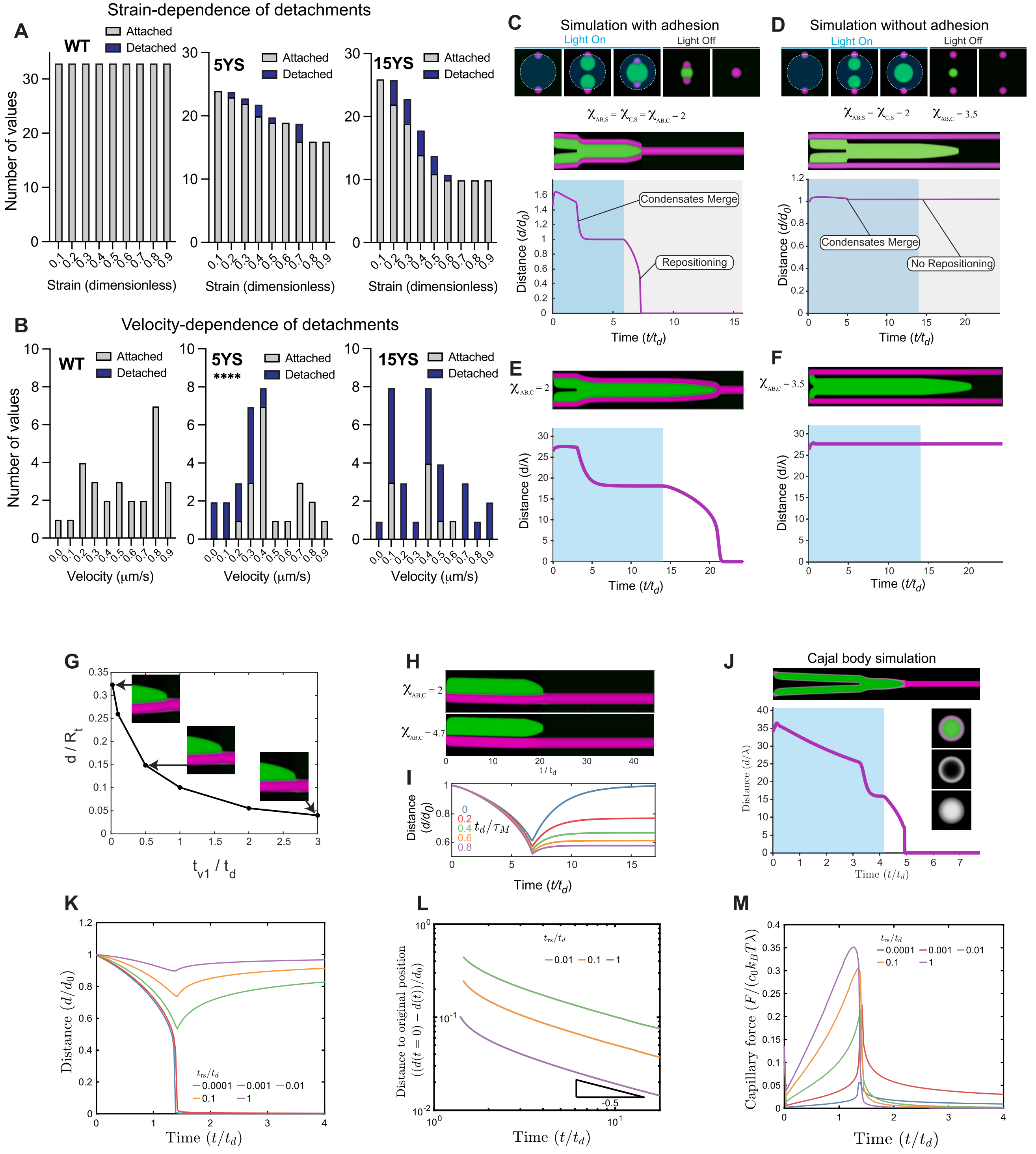

Figure S4. Simulations mimic adhesion-dependent loci repositioning by light-inducible condensates, related to Figure 4

(A and B) Experimental locus-condensate detachment probability plotted as a function of strain $(d_0 - d_d)/d_0$ (A) and locus movement velocity (B) for loci attached to FUS$_N^{WT}$ condensates by FUS$_N^{WT}$-, FUS$_N^{5YS}$-, and FUS$_N^{15YS}$-miRFP670-TRF1 (indicated as WT, 5YS, and 15YS). Strain trends are not statistically significant, 5YS chi-squared test for trend $p = 0.784$; 15YS $p = 0.436$. Velocity trend is statistically significant for 5YS, chi-squared test ****$p = 0.0004$, but not for 15YS $p = 0.498$.

(C) Simulation images, kymograph, and distance over time plot of growing and dissolving a central condensate (green) in a two-phase system with adhesion are able to recreate condensate-based repositioning of the second phase (magenta).

(legend continued on next page)

(D) Without adhesion, the simulated second phase is not repositioned, in line with experiments.

(E and F) The kymograph and distance between the centers of the telomere loci using identical parameters except for (E) $\chi_{AB,C} = 2$ and (F) $\chi_{AB,C} = 3.5$.

(G) Length of telomere displacement normalized by initial telomere radius R_t as a function of t_{v1}/t_d.

(H) Kymograph of Corelet nucleation and dissolution when it is next to a single telomere, while $\chi_{AB,C} = 2$ (top) and $\chi_{AB,C} = 4.7$ (bottom).

(I) The distance between two telomeres (normalized by their distance at the moment the light is turned off) over time as the Corelet condensate dissolves at various t_d/τ_M, using a viscoelastic liquid (Jeffreys) model. When telomeres detach from the condensate, they recoil.

(J) Kymograph and distance between Cajal bodies over time in simulation with no interaction kernel, thus the "Coilin" (magenta) is distributed over the surface of the Corelet condensate (green).

(K) Simulated distance between two telomeres using a Rouse polymer model of viscoelastic resistance to locus movement. Distance initially decreases as the condensate dissolves and pulls both telomeres toward each other, but as the resistance (t_{rs}/t_d) increases, telomeres recoil. For $t_{rs}/t_d \leq 0.01$, telomeres detach from the Corelet condensate and recoil at about $t/t_d = 1.4$. For $t/t_d \geq 0.1$, telomeres merge.

(L) Log-log plot of distance to original starting position as a function of time during recoil. Recoil dynamics follow $d(t = 0) - d(t) \propto t^{-1/2}$.

(M) Capillary force applied on telomere loci when they are pulled toward each other over time. Upon condensate dissolution, the pull force increases with increasing resistance of the polymer chain (t_{rs}/t_d).

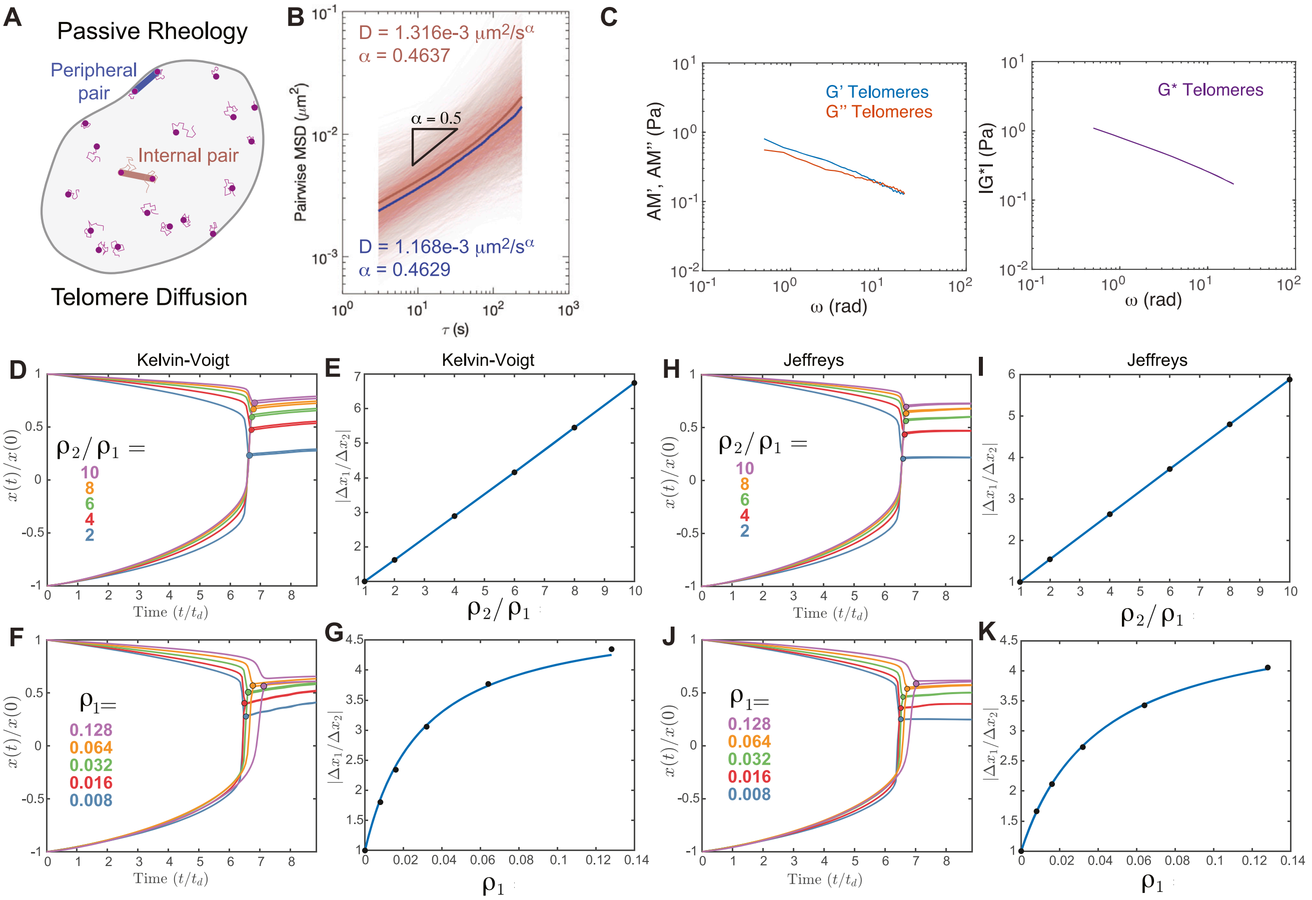

Figure S5. Rheological measurements and simulations of chromatin material state, related to Figure 5

(A) Schematic of definitions of peripheral (blue) and internal (mauve) pairs of telomeres for passive microrheological mean squared displacement (MSD) analysis.

(B) Averaged MSD trajectories (bold) of internal (mauve) or peripheral (blue) of pairs of diffusing telomeres. Log_{10} timestep in seconds, n = 2,408 internal pair trajectories and 51 peripheral pair trajectories from N = 31 cells.

(C–K) (C) Apparent moduli (AM) of elastic (AM′) and viscous (AM″) components of chromatin viscoelasticity calculated from MSD traces (left). Viscoelastic modulus G* obtained from apparent moduli (right). Using the Kelvin-Voigt model with $\tau_1/t_d = \tau_2/t_d = 2$, (D) the trajectories of the two telomeres $x(t)$ during the dissolution of the Corelet droplet and (E) the ratio of displacement of the two telomeres as a function of ρ_2/ρ_1 with fixed $\rho_1 = 0.05$. The displacement is defined to be the distance between the telomere position at t = 0 and its position at the moment when the two telomeres merge, indicated by the filled circles in (D). The values of the displacement ratio $|\Delta x_1/\Delta x_2|$ as shown as black dots in (E). Also using the Kelvin-Voigt model, (F) and (G) are the trajectories and ratio of displacement as a function of ρ_1 with fixed $\rho_2/\rho_1 = 5$. Using the Jeffreys model with $\tau_1/t_d = \tau_2/t_d = 2$ and $\tau_{M,1}/t_d = \tau_{M,2}/t_d = 2$, (H) and (I) are the trajectories and ratio of displacement as a function of ρ_2/ρ_1 with fixed $\rho_1 = 0.05$, (J) and (K) as a function of ρ_1 with fixed $\rho_2/\rho_1 = 5$. The blue lines and curves in (E), (G), (I), and (K) are fitted to the black data points using Equation 21 (see STAR Methods).

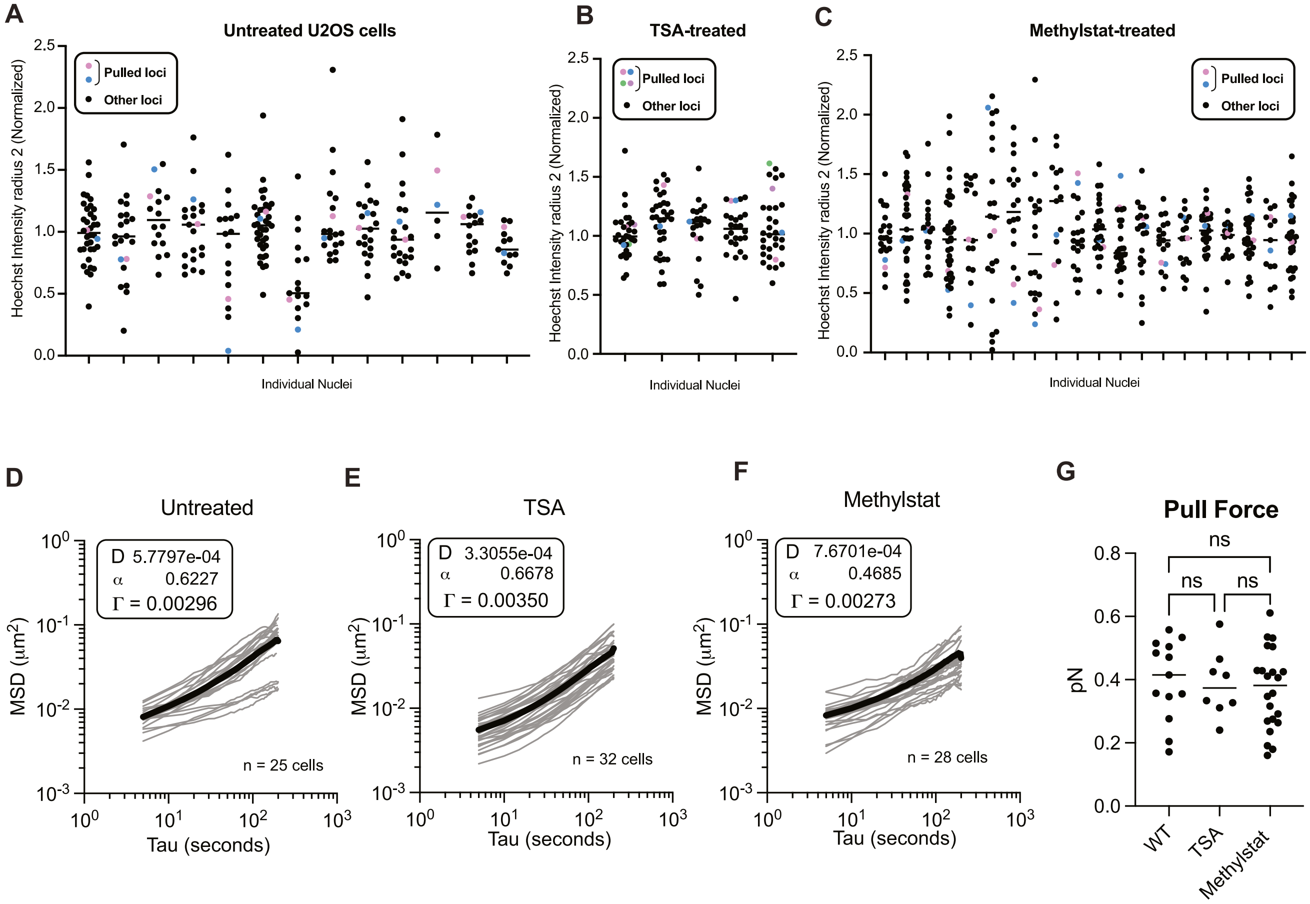

Figure S6. DNA density and passive locus diffusion are modified by epigenetic inhibitors, related to Figure 6

(A) Plot of Hoechst intensity in a 2-pixel (0.33 μm) radius circle ROI around each telomere, normalized to average nuclear Hoechst intensity in untreated cells. Pulled loci are shown in color, and all other telomeres are shown in black.

(B) Hoechst intensity around telomere loci in TSA-treated cells, showing smaller spread of intensity differences. In one nucleus, two pairs of loci were pulled and are shown in green/purple and pink/blue.

(C–F) (C) Hoechst intensity around telomere loci in methylstat-treated cells, showing increased spread in intensity differences. Mean squared displacement of telomeric loci pair trajectories in (D) untreated (*n* = 25 cells), (E) TSA-treated (*n* = 32 cells), and (F) methylstat-treated (*n* = 28 cells) nuclei. Gamma (Γ), calculated as $\langle x^2(t)\rangle = \Gamma\sqrt{t}$ is used to calibrate the force estimation model.

(G) Graph of the magnitude of force estimated for each pull across untreated, TSA-treated, and methylstat-treated cells using the Rouse polymer-based model.